Arch Appl Mech (2011) 81: 975–997
DOI 10.1007/s00419-010-0462-3

ORIGINAL

Jörg Schröder · Daniel Balzani · Dominik Brands

Approximation of random microstructures by periodic statistically similar representative volume elements based on lineal-path functions

Received: 3 May 2010 / Accepted: 29 June 2010 / Published online: 24 July 2010

Abstract For the direct incorporation of micromechanical information into macroscopic boundary value problems, the FE^2-method provides a suitable numerical framework. Here, an additional microscopic boundary value problem, based on evaluations of representative volume elements (RVEs), is attached to each Gauss point of the discretized macrostructure. However, for real random heterogeneous microstructures the choice of a "large" RVE with a huge number of inclusions is much too time-consuming for the simulation of complex macroscopic boundary value problems, especially when history-dependent constitutive laws are adapted for the description of individual phases of the mircostructure. Therefore, we propose a method for the construction of statistically similar RVEs (SSRVEs), which have much less complexity but reflect the essential morphological attributes of the microscale. If this procedure is prosperous, we arrive at the conclusion that the SSRVEs can be discretized with significantly less degrees of freedom than the original microstructure. The basic idea for the design of such SSRVEs is to minimize a least-square functional taking into account suitable statistical measures, which characterize the inclusion morphology. It turns out that the combination of the volume fraction and the spectral density seems not to be sufficient. Therefore, a hybrid reconstruction method, which takes into account the lineal-path function additionally, is proposed that yields promising realizations of the SSRVEs. In order to demonstrate the performance of the proposed procedure, we analyze several representative numerical examples.

Keywords Numerical homogenization · Random microstructure · Statistically similar RVE · Lineal-path function · Spectral-density · Finite plasticity

1 Introduction

Many modern engineering applications make use of advanced high-strength steels due to their high ductility and strength. In automotive construction, for instance, the reduction of weight in addition to an enhanced crash safety can be achieved by deploying these steels. The advantageous macroscopic material behavior is mainly governed by a complex interplay between the individual constituents at the microscale. However, the interactions of the individual phases of the micro-heterogeneous composites could lead to complicated macroscopic hardening effects. Furthermore, macroscopic failure analysis becomes sophisticated because failure initiation at the microscale usually appears already before a macroscopic failure may be observed.
For the computer simulation of structural problems, where such random heterogeneous materials are used at the microscale, two-scale modeling approaches are suitable algorithmic tools in order to capture the essential microscopic phenomena. In general, a sufficiently large section of the microscale, which acts here per definition as a representative volume element (RVE), is used for the approximation of the random microstructure.

J. Schröder (✉) · D. Balzani · D. Brands
Fakultät für Ingenieurwissenschaften, Institut für Mechanik, Abteilung Bauwissenschaften,
Universität Duisburg-Essen, Universitätsstr. 15, 45117 Essen, Germany
E-mail: j.schroeder@uni-due.de

This RVE is attached to each point of the macroscale. The numerical treatment of this approach is known as the direct micro-macro-transition procedure, the multilevel finite-element method or the FE^2-method, see e.g. Smit et al. [27], Brekelmans et al. [4], Miehe et al. [15–17], Schröder [22] and Geers et al. [7]. In this framework, a microscopic boundary value problem, where the geometry is characterized by RVEs, is solved at each integration point of the discretized macroscopic boundary value problem. Basic ideas for the direct micro-macro-transition approach with the application to DP-steels taking into account eigenstress distributions are given in Schröder et al. [23]. The main drawbacks of direct micro-macro approaches are the high computation time and the large amount of memory needed, when we deal with complex RVEs. Unfortunately, this is usually the case for micro-heterogeneous steels as e.g. DP-steels, when a substructure of a real micrograph serves as the RVE. In order to circumvent these drawbacks, the construction of statistically similar representative volume elements (SSRVEs), which are characterized by a much less complexity than a usual RVE, seems to be promissing.

Povirk [21] proposed a method for the construction of simplified RVEs as an approximation for a composite consisting of a matrix and randomly distributed equal circular inclusions. Here, a least-square functional has to be minimized, which compares the spectral densities of the original microstructure with the one of the simplified RVE. It should be noted that the spectral density is strongly correlated with the two-point probability function, cf. Zeman [33]. Further statistical measures are various scalar-valued parameters, n-point probability functions, lineal-path functions, and others, see Torquato [29].

Basic ideas for the procedure proposed here are to use spline approximations for the inclusion geometries and to consider a series of statistical measures in order to construct suitable SSRVEs. These SSRVEs should be able to approximate random inclusion-matrix microstructures in the sense that they yield similar macroscopic stress–strain curves compared with the ones obtained by the usage of large RVEs. The SSRVEs are obtained by minimizing least-square functionals, which compare the statistical measures of a given random microstructure with the ones of the SSRVE, cf. Balzani et al. [2]. A minimization algorithm for the resulting non-smooth optimization problem is proposed in Balzani et al. [1]. There, also the influence of the volume fraction, the specific internal surface density and the specific integral of mean curvature is compared with the impact of the spectral density. Obviously, it turns out that the simple scalar-valued measures are not sufficient for the description of the inclusion phase morphology. Although the spectral density captures directional-dependent information, it does not lead to satisfying results. Therefore, in this contribution, we improve the SSRVE construction method by restraining the parameterization process and by including further statistical information. It is shown that the additional incorporation of the lineal-path function provides significant improvements with respect to the mechanical representability of the SSRVEs.

The paper is organized as follows. First, the direct micro-macro modeling approach is shortly recapitulated and aspects for efficient computations of the macroscopic effective tangent moduli are explained. Section 3 provides a detailed description for the statistical measures related with the analysis performed here and explains how the numerical calculation of the measures can be improved. In Sect. 4, the method for the construction of SSRVEs is described, where also technical details for the construction of periodic unitcell type SSRVEs are given. Section 5 analyzes the influence of the spectral density and the lineal-path function with respect to the mechanical response of the resulting SSRVEs and provides a comparative analysis with respect to the mechanical response for macroscopic boundary value problems, whereas the last section concludes the paper.

2 Direct micro-macro modeling

In the computational two-scale homogenization procedure, we attach at each Gauss point of the discretized macroscopic boundary value problem a RVE, representing the underlying microstructure. Thus, we need no explicit constitutive equations for the description of the material behavior at the macroscale. This is given by volume averages of the first Piola-Kirchhoff stresses performed with respect to the RVE. Furthermore, the deformation of the RVE is driven by some energetically consistent boundary conditions, derived from the well-known Hill condition. In order to achieve a quadratic convergence within a Newton-Raphson iteration scheme for the macroscopic boundary value problem, a consistent linearization of the macroscopic first Piola-Kirchhoff stresses have to be performed, taking into account the discretized fluctuations on the RVE.

2.1 Deformation gradients and stresses at different scales

Let $\mathcal{B} \subset \mathbb{R}^3$ denote the body of interest at the microscale in its reference configuration at time $t = t_0$, parameterized in $\boldsymbol{X}$, wherein $\mathbb{R}^3$ is the Euclidian three-dimensional space. The actual configuration is denoted by $\mathcal{S} \subset \mathbb{R}^3$, parameterized in $\boldsymbol{x}$ at a fixed time $t \in \mathbb{R}_+$. Concentrating on the Boltzman continuum theory, the deformation of the body can be interpreted as the translational motion of material points. The non-linear, continuous, and one-to-one transformation $\boldsymbol{\varphi}(\boldsymbol{X}, t) : \mathcal{B} \to \mathcal{S}$ at time $t \in \mathbb{R}_+$ maps points $\boldsymbol{X} \in \mathcal{B}$ of the microscopic reference configuration onto points $\boldsymbol{x} \in \mathcal{S}$ of the actual microscopic configuration. For the description of deformations, we define the microscopic deformation gradient

$$\boldsymbol{F}(\boldsymbol{X}) := \mathrm{Grad}[\boldsymbol{\varphi}_t(\boldsymbol{X})], \tag{1}$$

with $J(\boldsymbol{X}) = \det[\boldsymbol{F}(\boldsymbol{X})] > 0$. The associated work-conjugated stress measure is the first Piola-Kirchhoff stress tensor $\boldsymbol{P}$, from which the microscopic Cauchy stresses and second Piola-Kirchhoff stresses can be computed by

$$\boldsymbol{\sigma} = \frac{1}{J}\, \boldsymbol{P}\, \boldsymbol{F}^T \quad \text{and} \quad \boldsymbol{S} = \boldsymbol{F}^{-1}\, \boldsymbol{P}, \tag{2}$$

respectively. At the macroscale, we use analogous notations and use overlined characters to identify macroscopic quantities, then we consider the transformation map $\overline{\boldsymbol{\varphi}}(\overline{\boldsymbol{X}}, t) : \overline{\mathcal{B}} \to \overline{\mathcal{S}}$ with the macroscopic physical bodies $\overline{\mathcal{B}}$ and $\overline{\mathcal{S}}$ in the reference and in the actual configuration, respectively. The macroscopic deformation gradient is defined by

$$\overline{\boldsymbol{F}}(\overline{\boldsymbol{X}}) := \mathrm{Grad}[\overline{\boldsymbol{\varphi}}_t(\overline{\boldsymbol{X}})], \tag{3}$$

with $\overline{J}(\overline{\boldsymbol{X}}) = \det[\overline{\boldsymbol{F}}(\overline{\boldsymbol{X}})] > 0$. Furthermore, the macroscopic Cauchy- and second Piola-Kirchhoff stresses are computed by

$$\overline{\boldsymbol{\sigma}} = \frac{1}{\overline{J}}\, \overline{\boldsymbol{P}}\, \overline{\boldsymbol{F}}^T \quad \text{and} \quad \overline{\boldsymbol{S}} = \overline{\boldsymbol{F}}^{-1}\, \overline{\boldsymbol{P}}. \tag{4}$$

2.2 Modeling of the individual phases at the microscale

For solving the boundary value problem on the microscale, constitutive equations for the individual phases on the microscale are required. During the deformation process, the composite exhibits large plastic deformations. Due to the lack of experiments, we apply an isotropic material behavior for both phases, the metallic matrix and the metallic inclusion. It seems to be reasonable to use an isotropic finite elastoplasticity formulation based on the multiplicative decomposition of the deformation gradient $\boldsymbol{F} = \boldsymbol{F}^e\, \boldsymbol{F}^p$ in elastic $\boldsymbol{F}^e$ and plastic $\boldsymbol{F}^p$ parts, see Kröner [10], Lee [12]. For details of the thermodynamical formulation as well as for the numerical treatment we refer to Simo [24,25], Simo and Miehe [26], Peric et al. [20], Miehe and Stein [18], and Miehe [14]. In the sequel, we provide a brief summary of the used framework. The basic kinematical quantities are

$$\boldsymbol{b} = \boldsymbol{F}\boldsymbol{F}^T = \boldsymbol{F}^e\, \boldsymbol{b}^p\, \boldsymbol{F}^{eT}, \quad \boldsymbol{b}^p = \boldsymbol{F}^p\, \boldsymbol{F}^{pT}, \text{ and } \quad \boldsymbol{b}^e = \boldsymbol{F}^e\, \boldsymbol{F}^{eT}, \tag{5}$$

with the spectral decomposition of the elastic finger tensor $\boldsymbol{b}^e = \sum_{A=1}^{3} (\lambda_A^e)^2 \boldsymbol{n}_A \otimes \boldsymbol{n}_A$. Herein, $\boldsymbol{n}_A$ denotes the eigenvectors and λ_A^e the eigenvalues of $\boldsymbol{b}^e$. The stored energy function is assumed to be of the form $\psi = \psi^e(\boldsymbol{b}^e) + \psi^p(\alpha)$. Following Simo [25], we use a quadratic free energy function

$$\psi^e = \frac{\lambda}{2}\left[\epsilon_1^e + \epsilon_2^e + \epsilon_3^e\right]^2 + \mu\left[(\epsilon_1^e)^2 + (\epsilon_2^e)^2 + (\epsilon_3^e)^2\right] \tag{6}$$

in terms of the logarithmic elastic strains $\epsilon_A^e = \log(\lambda_A^e)$; λ and μ are the Lamé constants. In order to model the individual phases with an exponential-type hardening, as in Voce [31], superimposed with a linear hardening, we apply the well-known function

$$\psi^p = y_\infty \alpha - \frac{1}{\eta}(y_0 - y_\infty)\exp(-\eta\alpha) + \frac{1}{2}\, h\, \alpha^2 \tag{7}$$

with the equivalent plastic strains α. However, the conjugated stress-like variable, defined as $\beta := \partial_\alpha \psi^p$, is

$$\beta = y_\infty + (y_0 - y_\infty)\exp(-\eta\alpha) + h\,\alpha. \tag{8}$$

This hardening function fits appropriately the experimental yield curves of purely ferritic and purely martensitic steels that have been used in the analysis here. Herein, y_0 is the initial yield strength, y_∞ and η describe an exponential hardening behavior and h is the slope of a superimposed linear hardening. The yield criterion reads

$$\phi = ||\mathrm{dev}\boldsymbol{\tau}|| - \sqrt{\frac{2}{3}}\beta \leq 0 \quad \text{with} \quad \boldsymbol{\tau} = \sum_{A=1}^{3} \tau_A\, \boldsymbol{n}_A \otimes \boldsymbol{n}_A \quad \text{and} \quad \tau_A = \frac{\partial \psi_e}{\partial \epsilon_e}. \tag{9}$$

The flow rule for the plastic quantity is integrated using an implicit exponential update algorithm, which preserves plastic incompressibility (Weber and Anand [32]; Simo [25]; Miehe and Stein [18]). The first Piola-Kirchhoff stresses on the microscale are computed by $\boldsymbol{P} = \boldsymbol{\tau}\,\boldsymbol{F}^{-T}$, cf. (2). For the numerical implementation, we follow the algorithmic formulation in a material setting as proposed in Klinkel [9].

2.3 Direct micro-macro homogenization scheme

On the microscale, we consider a RVE, parametrized in $\boldsymbol{X} \in \mathcal{B}$, where the microscopic field quantities have to be determined. The governing field equation is the balance of linear momentum for the quasi-static case, i.e. $\mathrm{Div}[\boldsymbol{P}] = \boldsymbol{0}$, where we have neglected the body forces on this scale.

For the direct (algorithmic) micro-macro transition, we must define relations between the deformation gradient and the first Piola-Kirchhoff stresses at the micro- and macroscale. In general, the macroscopic deformation gradient $\overline{\boldsymbol{F}}$ and the macroscopic first Piola-Kirchhoff stresses $\overline{\boldsymbol{P}}$ are defined by suitable surface integrals

$$\overline{\boldsymbol{F}} = \frac{1}{\mathrm{vol(RVE)}} \int_{\partial\mathcal{B}} \boldsymbol{x} \otimes \boldsymbol{N}\, \mathrm{d}A \quad \text{and} \quad \overline{\boldsymbol{P}} = \frac{1}{\mathrm{vol(RVE)}} \int_{\partial\mathcal{B}} \boldsymbol{t}_0 \otimes \boldsymbol{X}\, \mathrm{d}A, \tag{10}$$

with the outward unit normal $\boldsymbol{N}$ and the traction vector $\boldsymbol{t}_0$ on the boundary $\partial\mathcal{B}$ of the RVE. Taking advantage of some suitable technical assumptions for our applications, the macroscopic quantities can also be computed by simple volumetric averages, i.e. $\overline{\boldsymbol{F}} = \int_{\mathcal{B}} \boldsymbol{F}\, \mathrm{d}V\, /\mathrm{vol(RVE)}$ and $\overline{\boldsymbol{P}} = \int_{\mathcal{B}} \boldsymbol{P}\, \mathrm{d}V\, /\mathrm{vol(RVE)}$.
The boundary conditions of the boundary value problem at the microscale are derived from the macro-homogeneity condition, also referred to as Hill–condition, see Hill [8]. It postulates that the macroscopic power is equal to the volumetric average of the microscopic power, i.e.

$$\overline{\boldsymbol{P}} \cdot \dot{\overline{\boldsymbol{F}}} = \frac{1}{\mathrm{vol(RVE)}} \int_{\mathcal{B}} \boldsymbol{P} \cdot \dot{\boldsymbol{F}}\, \mathrm{d}V. \tag{11}$$

Possible boundary conditions are (i) the stress boundary condition, (ii) the linear boundary displacements, and (iii) periodic boundary conditions:

$$\text{(i)} \quad \boldsymbol{t}_0 = \overline{\boldsymbol{P}}\boldsymbol{N} \text{ on } \partial\mathcal{B}, \qquad \text{(ii)} \quad \boldsymbol{x} = \overline{\boldsymbol{F}}\boldsymbol{X} \text{ on } \partial\mathcal{B} \tag{12}$$

and

$$\text{(iii)} \quad \boldsymbol{x} = \overline{\boldsymbol{F}}\boldsymbol{X} + \widetilde{\boldsymbol{w}}, \quad \widetilde{\boldsymbol{w}}^+ = \widetilde{\boldsymbol{w}}^-, \quad \boldsymbol{t}_0^+ = -\boldsymbol{t}_0^- \text{ on } \partial\mathcal{B}. \tag{13}$$

Note that $\widetilde{\boldsymbol{w}}$ denotes fluctuations of the displacement field and that $(\bullet)^+$, $(\bullet)^-$ means quantities at periodically associated points of the RVE-boundary, for further details we refer to Miehe et al. [17], Schröder [22] and the references therein. The basic idea of the FE^2-method is that a microscopic boundary value problem is solved at each Gauss point of a macroscopic boundary value problem. Focussing on linear boundary displacements (ii) and periodic boundary conditions (iii), we additively split the microscopic deformation gradient in

the constant macroscopic part and a solely fluctuating part, i.e. $\boldsymbol{F} = \overline{\boldsymbol{F}} + \widetilde{\boldsymbol{F}}$, with $\widetilde{\boldsymbol{F}} = \mathrm{Grad}[\widetilde{\boldsymbol{w}}(\boldsymbol{X})]$. At the microscale, we consider the weak form and its linear increment for a typical finite element $\mathcal{B}^e$:

$$G^e(\widetilde{\boldsymbol{F}}, \delta\widetilde{\boldsymbol{F}}) = \int_{\mathcal{B}^e} \delta\widetilde{\boldsymbol{F}} \cdot \boldsymbol{P}\, \mathrm{d}V \quad \text{and} \quad \Delta G^e(\widetilde{\boldsymbol{F}}, \delta\widetilde{\boldsymbol{F}}, \Delta\widetilde{\boldsymbol{F}}) = \int_{\mathcal{B}^e} \delta\widetilde{\boldsymbol{F}} \cdot (\mathbb{A} : \Delta\widetilde{\boldsymbol{F}})\, \mathrm{d}V, \tag{14}$$

with the microscopic nominal moduli $\mathbb{A} := \partial_F \boldsymbol{P}$. The fluctuation parts of the actual, virtual, and incremental deformation gradient $\widetilde{\boldsymbol{F}}$, $\delta\widetilde{\boldsymbol{F}}$, and $\Delta\widetilde{\boldsymbol{F}}$, respectively, can be approximated by using standard ansatz functions for the fluctuations. Thus, we get the approximations $\widetilde{\boldsymbol{F}} = \boldsymbol{B}\,\widetilde{\boldsymbol{d}}$, $\delta\widetilde{\boldsymbol{F}} = \boldsymbol{B}\,\delta\widetilde{\boldsymbol{d}}$, $\Delta\widetilde{\boldsymbol{F}} = \boldsymbol{B}\,\Delta\widetilde{\boldsymbol{d}}$, with the standard B-matrix $\boldsymbol{B}$ and the discrete nodal fluctuations for the displacements $\widetilde{\boldsymbol{d}}$, virtual displacements $\delta\widetilde{\boldsymbol{d}}$, and incremental displacements $\Delta\widetilde{\boldsymbol{d}}$. After the standard assembling procedure, we obtain the discrete representation of the linearized problem

$$\delta\widetilde{\boldsymbol{D}}^T\{\boldsymbol{K}\,\Delta\widetilde{\boldsymbol{D}} + \boldsymbol{R}\} = 0, \tag{15}$$

with the global vectors of incremental fluctuations $\widetilde{\boldsymbol{D}}$, residual forces $\boldsymbol{R}$, and the global microscopic stiffness matrix $\boldsymbol{K}$. In each iteration, the actual increments of displacement fluctuations are computed from (15) and updated, i.e. $\widetilde{\boldsymbol{D}} \Leftarrow \widetilde{\boldsymbol{D}} + \Delta\widetilde{\boldsymbol{D}}$, until $|\boldsymbol{R}| < \mathrm{tol}$, where tol represents the algorithmic tolerance. When a converged solution of the microscopic BVP is obtained, the volume average of the resulting microscopic stresses $\overline{\boldsymbol{P}}$ is transferred to the macroscale. Now, we have to solve the BVP on the macroscale, which is quite standard and therefore not reflected here. Nevertheless, one crucial point has to be solved during this homogenization step in order to achieve a quadratic convergence for the solution procedure of the discrete macroscopic BVP within a classical Newton-Raphson iteration scheme. We have to compute the algorithmic consistent macroscopic (overall) incremental response of the material nominal moduli $\overline{\mathbb{A}} := \partial_{\overline{F}}\overline{\boldsymbol{P}}$, which enters the incremental relation $\Delta\overline{\boldsymbol{P}} = \overline{\mathbb{A}} : \Delta\overline{\boldsymbol{F}}$. The overall moduli are computed by

$$\overline{\mathbb{A}} = \langle\mathbb{A}\rangle - \frac{1}{\mathrm{vol(RVE)}}\boldsymbol{L}^T\boldsymbol{K}^{-1}\boldsymbol{L} \tag{16}$$

with

$$\langle\mathbb{A}\rangle = \frac{1}{\mathrm{vol(RVE)}}\int_{\mathcal{B}} \mathbb{A}\,\mathrm{d}V \quad \text{and} \quad \boldsymbol{L} = \mathop{\mathbf{A}}_{e=1}^{n_{ele}} \int_{\mathcal{B}^e} \boldsymbol{B}^T\mathbb{A}\,\mathrm{d}V, \tag{17}$$

where the first term denotes the classical Voigt bound and the second term acts as a softening term. For details on deriving the consistent macroscopic moduli, see Miehe et al. [15] and Schröder [22], in this context see also Miehe et al. [17], Temizer and Wriggers [28].

3 Statistical measures for microstructure characterization

Considering micro-heterogeneous materials, the continuum mechanical properties at the macroscale are characterized by the morphology and by the properties of the particular constituents at the microscale. In this contribution, microstructures are considered which consist of an inclusion phase embedded in a matrix phase. The material behavior of the individual constituents is assumed to be known and obtained by experiments on homogeneous specimens made of single-phase materials. Then, the description of the microstructure is based on statistical considerations, see the basic literature in e.g. Beran [3] and Kröner [11]. Due to the fact that we focus on two-phase microstructures, we concentrate on measures characterizing the inclusion phase, if it is not specified otherwise, since the measures computed for the matrix will be dependent in general.

3.1 Basic parameters

For the description of microstructure morphology, there exist four basic parameters, see e.g. Ohser and Mücklich [19]. In the general three-dimensional case, the first two parameters are defined by

$$\mathcal{P}_V^{(i)} := \frac{V_{(i)}}{V} \quad \text{and} \quad \mathcal{P}_S^{(i)} := \frac{S_{(i)}}{V}, \tag{18}$$

with the volume $V_{(i)}$ of the phase i and the interface area $S_{(i)}$ separating phase i from the residue of the microstructure. In order to obtain specific quantities, the division by the total volume of the considered material segment V is taken into account. These two parameters basically represent the volume fraction (or phase fraction) and the specific internal surface density. It is emphasized that the volume fraction is an essential property which should be matched by all considered RVEs, whereas the specific internal surface density provides information with respect how fine an inclusion phase is distributed. The third parameter, the specific integral of mean curvature

$$\mathcal{P}_M := \frac{1}{2V} \int_S \left(\min_\beta[\kappa] + \max_\beta[\kappa] \right) \mathrm{d}s, \tag{19}$$

is defined by the integral over the surface S between the individual phases, $\kappa := \kappa(\beta)$ denotes the curvature and β the direction in the tangential plane. The fourth parameter

$$\mathcal{P}_K := \frac{1}{V} \int_S \min_\beta[\kappa] \, \max_\beta[\kappa] \, \mathrm{d}s \tag{20}$$

is the specific integral of total curvature. The latter two parameters provide in some sense statistical information concerning the degree of curvature of the inclusion phase. Although these four parameters are widely used for the description of microstructures, they are obviously not able to cover direction-dependent information since they are scalar valued. This is required for the representation of oriented inclusions leading to an overall anisotropy. It is shown in Balzani et al. [1] that the basic parameters alone are not sufficient for the construction of statistically similar RVEs. Therefore, statistical measures of higher order are required.

3.2 n-point probability functions

Originally, n-point probability functions have been used for the determination of effective dielectric constants in two-phase random media. These functions have been introduced by Brown [6], and important applications with respect to effective elastic moduli are given in e.g. Beran [3].
Let $D^{(i)}(\alpha)$ denote the domain occupied by the considered phase i in the particular sample α, then the indicator function reads

$$\chi^{(i)}(\boldsymbol{x}, \alpha) = \begin{cases} 1, & \text{if } \boldsymbol{x} \in D^{(i)}(\alpha), \\ 0, & \text{otherwise}, \end{cases} \tag{21}$$

with the general property for n phases $\sum_{i=1}^{n} \chi^{(i)}(\boldsymbol{x}, \alpha) = 1$, for every point $\boldsymbol{x}$. The general n-point probability function, which is also referred to as n-point correlation function, is defined by the ensemble average

$$\mathcal{S}_n^{(1,\dots n)}(\boldsymbol{x}_1, \dots \boldsymbol{x}_n) = \overline{\chi^{(1)}(\boldsymbol{x}_1, \alpha) \chi^{(2)}(\boldsymbol{x}_2, \alpha) \dots \chi^{(n)}(\boldsymbol{x}_n, \alpha)}, \tag{22}$$

which represents the probability that the points $\boldsymbol{x}_1, \dots \boldsymbol{x}_n$ are located in the phases $D^{(1)}, \dots D^{(n)}$. With respect to two-phase microstructures, the main interest concerns the description of the inclusion phase, then one considers the representation

$$\mathcal{S}_n^{I}(\boldsymbol{x}_1, \dots \boldsymbol{x}_n) = \overline{\chi^{I}(\boldsymbol{x}_1, \alpha) \chi^{I}(\boldsymbol{x}_2, \alpha) \dots \chi^{I}(\boldsymbol{x}_n, \alpha)}, \tag{23}$$

characterizing the probability that all n points $\boldsymbol{x}_1, \dots \boldsymbol{x}_n$ are located in the inclusion phase. In general, it is possible, to compute the n-point probability function for one phase in terms of the other one, cf. Torquato & Stell [30]. Generally, a microstructure can be completely described if the set of all probability functions $\mathcal{S}_1^{(1,\dots n)}, \mathcal{S}_2^{(1,\dots n)}, \dots \mathcal{S}_n^{(1,\dots n)}$ for $n \to \infty$ is taken into account. This is of course impossible to be computed practically since it represents an infinite number of measures calculated for an infinite number of multiple positions. Therefore, we focus on some "lower"-order probability functions in order to obtain sufficient information for the microstructure characterization.

The probability function of first order (one-point probability function) is given by

$$\mathcal{S}_1^{(i)}(\boldsymbol{x}) = \overline{\chi^{(i)}(\boldsymbol{x}, \alpha)}, \tag{24}$$

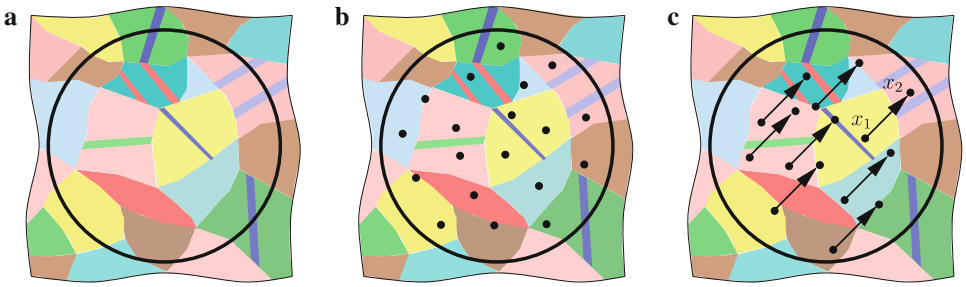

Fig. 1 **a** Multi-phase microstructure and illustration of the **b** one-point probability function, and **c** of the two-point probability function

representing the probability that a point $\boldsymbol{x}$ is placed in phase i. The one-point probability function coincides with the first basic parameter, the phase fraction. For an illustration of the calculation of the one-point probability function for a multi-phase material see Fig. 1b.

If the binary image of $N = N_x \times N_y$ pixels of one representative sample of an ergodic inclusion-matrix microstructure is analyzed, then the one-point probability function for the inclusion phase is computed by

$$\mathcal{P}_V = \mathcal{S}_1^I = \frac{1}{N_x N_y} \sum_{p=0}^{N_x-1} \sum_{q=0}^{N_y-1} \chi^I(p,q) \tag{25}$$

wherein p and q represent the pixel positions in the binary image. Of course, the evaluation of this summation leads to the exact value of first-order probability since all possible positions are evaluated. However, in most cases it is more efficient to only evaluate Eq. (25) at a sufficient number $N^r < N$ of random positions and then the equation

$$\mathcal{S}_1^I = \lim_{N^r \to N} \left[\frac{1}{N^r} \sum_{j=0}^{N^r} \chi^I(p_j, q_j) \right] \tag{26}$$

holds. Herein, the pixel positions for each random generation j are denoted by p_j and q_j.

The second-order function (two-point probability or autocorrelation function) is generally given by the ensemble average

$$\mathcal{S}_2^{(1,2)}(\boldsymbol{x}_1, \boldsymbol{x}_2) = \overline{\chi^{(1)}(\boldsymbol{x}_1, \alpha)\chi^{(2)}(\boldsymbol{x}_2, \alpha)} \tag{27}$$

over all samples α. This characterizes the probability that a point $\boldsymbol{x}_1$ is located in phase 1 and point $\boldsymbol{x}_2$ in phase 2. With respect to statistically homogeneous two-phase materials, where the position itself of two points is not important, but rather the relative position of one point to another, it is more reasonable to compute the alternative form

$$\mathcal{S}_2^I(\boldsymbol{y}) = \overline{\chi^I(\boldsymbol{x}(\alpha), \alpha)\chi^I(\boldsymbol{x}(\alpha) + \boldsymbol{y}, \alpha)}. \tag{28}$$

as the ensemble average over all samples α. This form does not depend on the global position of two points but rather on the relative position. It describes the probability that the points $\boldsymbol{x}(\alpha)$, which is allowed to vary from sample to sample, and $\boldsymbol{x}(\alpha) + \boldsymbol{y}$ are located in the inclusion phase, cf. Fig. 1c. When evaluating the two-point probability function for the inclusion phase in a binary image of an ergodic two-phase microstructure with a number of $N = N_x \times N_y$ pixels, the discrete representation

$$\mathcal{S}_2^I(m,k) = \frac{1}{(p_M - p_m)(q_K - q_k)} \sum_{p=p_m}^{p_M-1} \sum_{q=q_k}^{q_K-1} \chi^I(p,q)\chi^I(p+m, q+k) \tag{29}$$

with the summation limits

$$\begin{aligned} p_m &= \max[0, -m], \quad & p_M &= \min[N_x, N_x - m] \\ q_k &= \max[0, -k], \quad & q_K &= \min[N_y, N_y - k] \end{aligned} \tag{30}$$

can be applied. Again, a more efficient method for the computation of the second-order probability function with a tolerable deviation is to evaluate only a suitable number of $N^r < N$ random points. For periodic microstructures, it is sufficient to consider only the periodic unitcell, then the two-point probability function is computed by

$$\mathcal{S}_2^I(m,k) = \frac{1}{N_x N_y} \sum_{p=1}^{N_x} \sum_{q=1}^{N_y} \chi^I(p,q)\chi^I(p+m,q+k). \tag{31}$$

For statistically homogeneous and isotropic microstructures, the n-point probability function is invariant with respect to the orientation of $\boldsymbol{y}$, and only the magnitudes play a role. Then, the second-order probability function reduces to $\mathcal{S}_2^I(y)$, wherein y is the length of the translational vector $\boldsymbol{y}$. Then, if the two-point probability function is computed for one representative sample of an ergodic microstructure by evaluating random pairs of points in a discrete sense, we consider the representation

$$\mathcal{S}_2^I(x_{mk}) = \frac{1}{N^r} \sum_{j=1}^{N^r} \chi^I(p_j,q_j)\chi^I(p_j+m_j,q_j+k_j), \tag{32}$$

with a reasonably defined difference magnitude $x_{mk} := x_{mk}(m_j,k_j)$ for vectors with integer coordinates and a number of random evaluations N^r.

3.3 Spectral density

An alternative approach for the characterization of microstructures, which is strongly correlated with the two-point probability function, is to compute the (discrete) spectral density for the inclusion phase of a binary image. For the calculation of the spectral density, we consider the indicator function defined in Eq. (21) and compute the (discrete) Fourier transform

$$\mathcal{F}^I(m,k) = \sum_{p=1}^{N_x} \sum_{q=1}^{N_y} \exp\left(\frac{2\,i\,\pi\,m\,p}{N_x}\right) \exp\left(\frac{2\,i\,\pi\,k\,q}{N_y}\right) \chi^I(p,q). \tag{33}$$

The maximal numbers of pixels in horizontal and vertical direction in the considered binary image are again given by N_x and N_y. Then, the discrete spectral density is computed by the multiplication of the discrete Fourier transform with its conjugate complex

$$\mathcal{P}_{\mathrm{SD}}(m,k) := \frac{1}{2\pi\, N_x\, N_y} |\mathcal{F}(m,k)|^2. \tag{34}$$

It is remarked that a strong correlation with the two-point probability function exists, since it can also be computed from the Fourier transform

$$\mathcal{S}_2^I(m,k) = \frac{1}{N_x\, N_y} (\mathcal{F}^I)^{-1}[\mathcal{F}^I[\chi^I(m,k)]\overline{\mathcal{F}^I[\chi^I(m,k,\alpha)]}], \tag{35}$$

cf. Zeman [33]. Herein, $\mathcal{F}^I$ and $(\mathcal{F}^I)^{-1}$ denote the discrete- and the inverse discrete Fourier transform following Eq. (33). This means that the spectral density covers in some sense information associated with the two-point probability function. However, direct information concerning the periodicity of a given microstructure is provided by the spectral density; thus, this measure may be of particular interest when the challenge is to simplify a (in general non-periodic) real microstructure by a periodic one. A main advantage of using the spectral density compared to the two-point probability function is that there exist a variety of efficient algorithms for the computation of the discrete Fourier transform as for instance the "FFTW" library, which stands for "Fastest Fourier Transform in the West", developed at the Massachusetts Institute of Technology by M. Frigo and S.G. Johnson.

3.4 Lineal-path function

Another statistical measure of higher order for the characterization of microstructure is the lineal-path function (also referred to as linear-path function), see Lu and Torquato [13]. This measure describes the probability that a complete line segment $\overrightarrow{\boldsymbol{x}_1\boldsymbol{x}_2}$ is located in the same phase. This is a rather practicable measure since its computation can be performed in an efficient way. For its mathematical description, we consider the modified indicator function

$$\chi^{(i)}(\overrightarrow{\boldsymbol{x}_1\boldsymbol{x}_2}, \alpha) = \begin{cases} 1, & \text{if } \overrightarrow{\boldsymbol{x}_1\boldsymbol{x}_2} \in D^{(i)}(\alpha), \\ 0, & \text{otherwise}, \end{cases} \tag{36}$$

simply checking if a whole line segment is located in the domain $D^{(i)}$ of phase i. Then, the general definition of a lineal-path function demands the computation of the ensemble average, and we get the definition

$$\mathcal{P}_{LP}^{(i)}(\overrightarrow{\boldsymbol{x}_1\boldsymbol{x}_2}) = \overline{\chi^{(i)}(\overrightarrow{\boldsymbol{x}_1\boldsymbol{x}_2}, \alpha)}, \tag{37}$$

compare the illustration shown in Fig. 2a,b.

For statistically homogeneous microstructures, the origin of the line segment vanishes, and the only dependency is on the orientation and length of the line segment. In this case, we are able to reformulate the alternative definition

$$\mathcal{P}_{\mathrm{LP}}^{(i)}(\boldsymbol{y}) = \overline{\chi^{(i)}(\overrightarrow{\boldsymbol{x}(\alpha)\boldsymbol{x}(\alpha) + \boldsymbol{y}}, \alpha)}, \tag{38}$$

wherein $\boldsymbol{y}$ denotes a vector representing the line segment $\overrightarrow{\boldsymbol{x}_1\boldsymbol{x}_2}$ independent on its point of application. If the microstructure to be analyzed is statistically homogeneous and statistically isotropic the definition reduces again to $\mathcal{P}_{\mathrm{LP}}^{(i)}(y)$, wherein y is the length of the line segment vector $\boldsymbol{y}$. An important extreme value of $\mathcal{P}_{\mathrm{LP}}^{(i)}(y)$ is $\lim_{y\to 0} \mathcal{P}_{\mathrm{LP}}^{(i)}(y) = \mathcal{P}_V$, showing that the lineal-path function becomes the phase fraction for vanishing magnitudes y.

For the calculation of lineal-path functions in two-dimensional discrete representations (binary images) of statistically homogeneous and ergodic inclusion-matrix microstructures, we analyze only one representative sample α and consider the modified definition for the indicator function

$$\chi^{I}(\boldsymbol{y}) = \begin{cases} 1, & \text{if } \overrightarrow{\boldsymbol{x}(\boldsymbol{x} + \boldsymbol{y})} \in D^{I}, \\ 0, & \text{otherwise}, \end{cases} \tag{39}$$

which is strongly associated with the form given in Eq. (38). For the discrete case, the lineal-path function is defined by

$$\mathcal{P}_{\mathrm{LP}}^{I}(m,k) = \frac{1}{(p_M - p_m)(q_K - q_k)} \sum_{p=p_m}^{p_M-1} \sum_{q=q_k}^{q_K-1} \chi^{I}(\tilde{\mathbf{y}}) \tag{40}$$

with the difference vector $\tilde{\mathbf{y}} = [p+m, q+k]^T$ and the summation limits

$$\begin{aligned} p_m &= \max[0, -m], \quad & p_M &= \min[N_x, N_x - m] \\ q_k &= \max[0, -k], \quad & q_K &= \min[N_y, N_y - k]. \end{aligned} \tag{41}$$

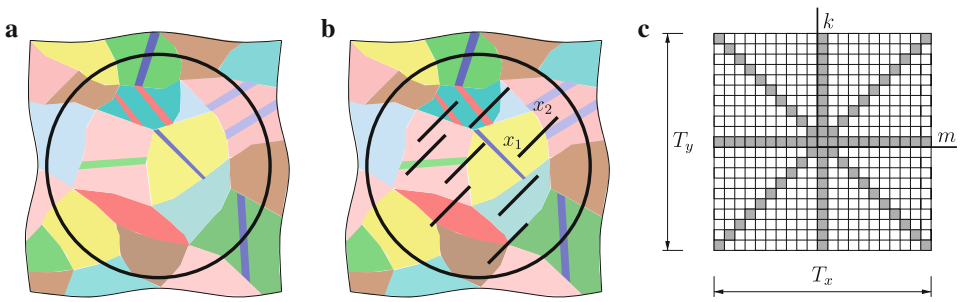

Fig. 2 **a** Multi-phase microstructure, **b** illustration of some representative lineal-path elements and **c** a typical template for the analyzed line directions $\beta_L = 0°, 45°, 90°, 135°$

For periodic unitcells, the lineal-path function is computed by

$$\mathcal{P}^I_{\mathrm{LP}}(m,k) = \frac{1}{N_x N_y} \sum_{p=1}^{N_x} \sum_{q=1}^{N_y} \chi^I(\tilde{\mathbf{y}}). \tag{42}$$

Efficient procedures for the calculation of the lineal-path function can be obtained by defining suitable templates, cf. Zeman [33]. Such a template consists of $T_x \times T_y$ pixels, wherein each pixel characterized by the coordinate pair (m, k) has either the value one or zero. The value one means that the associated line segment defined by the difference vector which ends in this coordinate pair (m, k) is part of the analysis. One example for a template is shown in Fig. 2c, where only the line segments in the horizontal -, vertical - and diagonal directions are analyzed. Then, each line segment defined by the template is compared with the original image for each admissible position (p, q). For the case under investigation here, the lineal-path function is invariant with respect to reflections of line segments. Hence, the lower half of the template shown in Fig. 2c is unnecessary. For binary images, each line segment to be analyzed has to be defined in an integer manner, which means that by given difference vector $\boldsymbol{y}$ a unique discrete line segment has to be constructed in the template. For this purpose, the classical Bresenham algorithm (Bresenham [5]) can be used.
If the complete lineal-path function has to be computed, the template needs to have the double size of the original binary image, e.g.

$$T_x = 2\,N_x - 1, \quad T_y = N_y, \tag{43}$$

and each pixel in the template needs to have the value one. Then, all possible line segments are analyzed. For the example shown in Fig. 2c, the original binary image has to have a minimal size of 11×11 pixels. Of course, in most cases it is not necessary to compute a complete lineal-path function. The first possibility to improve the efficiency of the algorithm is to reduce the size of the template according to a characteristic maximal inclusion size. A second possibility is to reduce the number of analyzed line segments; in most cases it will be sufficient to analyze only a certain set of line orientations. As a third possibility, it can be remarked that it may not be necessary to evaluate the indicator function for all positions in the original image. It may be sufficient to place the line segments defined in the template at a random position and repeat this process a number of N^r times, then the discrete form of the lineal-path function reads

$$\mathcal{P}^I_{\mathrm{LP}}(m,k) = \frac{1}{N^r} \sum_{j=1}^{N^r} \chi^I(\tilde{\mathbf{y}}_j) \tag{44}$$

with the difference vector $\tilde{\mathbf{y}}_j = [p_j + m, q_j + k]^T$. The random positions represented by the coordinates (p_j, q_j) have to fulfill

$$\begin{aligned} \max[0, -m] &\le p_j \le \min[N_x, N_x - m] - 1 \\ \max[0, -k] &\le q_j \le \min[N_y, N_y - k] - 1 \end{aligned} \tag{45}$$

for random microstructures and

$$1 \le p_j \le N_x \quad \text{and} \quad 1 \le q_j \le N_y \tag{46}$$

for periodic unitcells. The sufficient number of random points N^r that have to be evaluated can be computed from standard statistics.

4 Construction of statistically similar RVEs

In most cases, a usual RVE for a random inclusion/matrix-microstructure is determined by the smallest possible sub-domain which is still able to represent the macroscopic material behavior in the context of direct micro-macro approaches. Although these RVEs are the smallest possible sub-structures, they could be too complex for efficient calculations. Therefore, the construction of statistically similar RVEs, which are characterized by a lower complexity than the smallest possible random sub-structures, is proposed here for the reduction of computational costs. The basic idea in this context is to replace a RVE with an arbitrary complex inclusion morphology by a periodic one composed of optimal periodically arranged unitcells, see Fig. 3. Then, the main

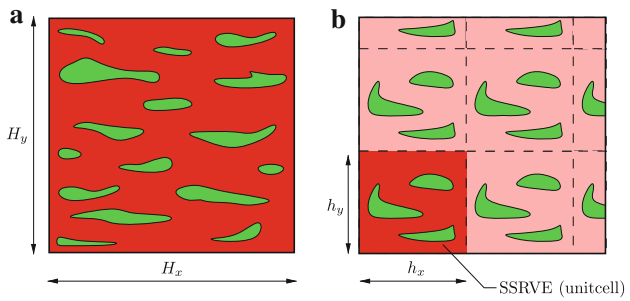

Fig. 3 Schematic illustration of the basic concept: **a** complex (non-periodic) RVE for a two-phase microstructure with arbitrary inclusion morphology and **b** simplified periodic microstructure with SSRVE

effort is that in FE^2 calculations only the periodic unitcell needs to be considered as a RVE provided that periodic boundary conditions are applied.

A method for the construction of such periodic structures is proposed for the special case of randomly distributed circular inclusions with constant equal diameters in Povirk [21]. The underlying idea there is to find the positions of circular inclusions with given diameter such that a least-square functional taking into account the side condition that the spectral density of the periodic RVE should be similar to one of the non-periodic microstructure is minimized. Motivated by this approach, we consider the objective function

$$\mathcal{L}(\boldsymbol{\gamma}) = \sum_{L=1}^{n_{\mathrm{sm}}} \omega_i \, \mathcal{L}_{\mathrm{SM}}^{(L)}(\boldsymbol{\gamma}) \rightarrow \min, \tag{47}$$

cf. Balzani et al. [2], which has to be minimized. A number of n_{sm} different statistical measures describing the inclusion morphology are taken into account by incorporating suitable least-square functionals. These functionals take into account the squares of differences in the individual statistical measures $\mathcal{P}_{(L)}^{real}$ and $\mathcal{P}_{(L)}^{\mathrm{SSRVE}}(\boldsymbol{\gamma})$ computed for a real (complex) microstructure and for the SSRVE. The weighting factor ω levels the influence of the individual measures. Due to the discrete character of the statistical measures entering the minimization problem (47), the energy surface is not smooth and therefore, no gradient-based optimization method can be applied. Therefore, the moving-frame algorithm proposed in Balzani et al. [1] is used. For the description of a general inclusion phase morphology in the SSRVE, we assume a suitable two-dimensional parameterization controlled by the vector $\boldsymbol{\gamma}$. In this work, splines are used for the parameterization; thus, the coordinates of the sampling points enter the general vector $\boldsymbol{\gamma}$

$$\boldsymbol{\gamma} := [\hat{x}_1 \, , \; \hat{y}_1 \, , \; \hat{x}_2 \, , \; \hat{y}_2, \ldots, \hat{x}_{n_{\mathrm{sp}}}, \; \hat{y}_{n_{\mathrm{sp}}}]^T \tag{48}$$

with the number of sampling points n_{sp}. Due to the fact that periodic boundary conditions have to be applied, the inclusions have to be constructed appropriately. For this purpose, the construction procedure is as follows: first, the number of inclusions and the number of sampling points are defined. Then, random positions of the sampling points are computed in a specified space $((N_x + 2\,f\,N_x) \times (N_y + 2\,f\,N_y))$ where a certain spatial overlap factor f with respect to the SSRVE space of interest $(N_x \times N_y)$ is taken into account. This means that the sampling point coordinates have to match

$$x_i \in [-f N_x, N_x + f N_x], \quad y_i \in [-f N_y, N_y + f N_y] \quad \text{for} \quad i = 1 \ldots n_{\mathrm{sp}}. \tag{49}$$

Here, we set the overlap factor to $f = 0.1$ and consider a SSRVE resolution of $N_x \times N_y = 60 \times 60$ pixels. The resulting splines are shown exemplarily in Fig. 4a as dark splines. Then, the SSRVE is periodically expanded by inserting the generated splines at the periodic positions, cf. the lighter splines in Fig. 4a. In order to preclude inclusions that intersect with themselves or with others, this construction procedure is repeated until a permitted unitcell is obtained and a resulting binary image of the SSRVE as shown in Fig. 4b is constructed.

If intersections of splines with themselves are not excluded, an unreasonable inclusion morphology leading to degenerated finite-element discretizations is generated if one spline consists of more than three sampling points. Convex inclusions are obtained if a spline has less than four sampling points.

As we have seen in preceding investigations (Balzani et al. [1,2]), the spectral density seems to be a suitable measure covering information concerning periodicity as well as macroscopic anisotropy, and it is relatively

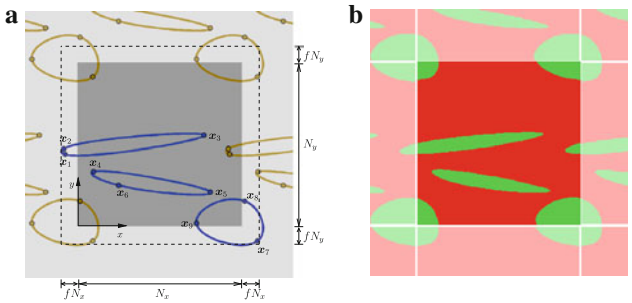

Fig. 4 Periodic unitcell construction based on splines: **a** required splines with the sampling points and **b** resulting binary SSRVE image (center) with the periodic expansion (brightend)

efficient to be computed compared to the complete two-point probability function. There, it has also been observed that simple basic parameters as the specific internal surface density and the specific integral of mean curvature are not suitable for the characterization of a complex microstructure. However, the phase fraction plays a key role and hence, we choose this statistical measures as well as the spectral density to be included in the objective function.

As already mentioned in Sect. 3, for an exact description of the microstructure one would need to take into account all n-point probability functions for $n = 1, \dots \infty$. But even if "only" a three-point probability function is considered as an additional measure, then the procedure will likewise be very expensive to be computed since the three-point probability function has a much higher dimension of solution space than the two-point probability function. Therefore, the lineal-path function may be a further reasonable statistical measure since it has the same solution space as the two-point probability function, and it covers further information with respect to the type of connectivity of points and therefore the connectedness of inclusions. This information is rather not covered by the spectral density. Conversely, information regarding relative distances between the inclusions cannot be represented by the lineal-path function but is one of the main features of the spectral density. In total, three different statistical measures are considered in this paper leading to the three individual least-square functionals:

$$\begin{aligned}
\mathcal{L}_V(\boldsymbol{\gamma}) &:= \left(1 - \frac{\mathcal{P}_V^{\text{SSRVE}}(\boldsymbol{\gamma})}{\mathcal{P}_V^{\text{real}}}\right)^2, \\
\mathcal{L}_{\text{SD}}(\boldsymbol{\gamma}) &:= \frac{1}{N_x\, N_y} \sum_{m=1}^{N_x} \sum_{k=1}^{N_y} \left(\mathcal{P}_{\text{SD}}^{\text{real}}(m,k) - \mathcal{P}_{\text{SD}}^{\text{SSRVE}}(m,k,\boldsymbol{\gamma})\right)^2, \\
\mathcal{L}_{\text{LP}}(\boldsymbol{\gamma}) &:= \frac{1}{N_x\, N_y} \sum_{m=1}^{N_x} \sum_{k=1}^{N_y} \left(\mathcal{P}_{\text{LP}}^{\text{real}}(m,k) - \mathcal{P}_{LP}^{\text{SSRVE}}(m,k,\boldsymbol{\gamma})\right)^2.
\end{aligned} \tag{50}$$

It is remarked that for the computation of the statistical measures $\mathcal{P}_{\text{SD}}$ and $\mathcal{P}_{\text{LP}}$ periodic expansions of the SSRVE are considered by putting as much SSRVEs as needed against each other periodically, cf. the brightened areas in Fig. 4b.

5 Comparative analysis

In order to check the performance of the proposed method and to analyze the influence of the individual statistical measures, SSRVEs are constructed in this section approximating a virtually generated target microstructure. Then, the mechanical response of the SSRVEs is compared in simple virtual experiments with the response of the target structure. To provide quantitative estimations for the accuracy of the individual considered least-square functionals, a mechanical error analysis is performed.

Limitations: In the following boundary value problems, we enforce plain stress conditions at each point of the microstructure. Furthermore, we assume that the individual phases can be described within the framework of the isotropic J_2-plasticity theory. Both assumptions are only approximations of the real material behavior. In a variety of micro-heterogeneous problems, the three-dimensional nature of the inclusion morphology

must be taken into account in order to capture the realistic macroscopic material behavior. However, from our experience with the analysis of thin steel plates the crucial plain stress assumption leads often to appropriate results when comparing with experimental data. Due to the fact that only uniaxial tension tests of the individual ferritic and martensitic steels have been available, the purely isotropic J_2-plasticity model was used.

5.1 Setup of virtual experiment

The virtual target microstructure is obtained by the Boolean method, where a certain two-dimensional space of interest is first completely filled with the inclusion phase. Then, ellipsoids with the semi-axis r_x and r_y of predefined aspect ratios, here $r_x/r_y = 14.3$, and random semi-axis $r_x \in [3, 6]\mu$m are randomly placed in the space of interest. This process is stopped if a certain phase fraction of $\mathcal{P}_V = 0.1872$ is reached. The resulting binary image is shown in Fig. 5a. Subsequently, the boundaries of the inclusion phase are smoothened, and a finite-element discretization is automatically generated, see Fig. 5b.

Here, 14982 triangular finite elements with quadratic ansatz functions for the displacements are taken into account. One main goal is to construct suitable SSRVEs that are characterized by a much less complexity than the target structure and that lead to a very similar mechanical response. For the construction of the SSRVEs, five different types are considered: Type I takes into account one inclusion with three sampling points, Type II one inclusion with four sampling points, Type III two inclusions with three sampling points each, Type IV two inclusions with four sampling points each, and Type V three inclusions with three sampling points each, cf. Fig. 6. Please note that splines with three sampling points lead to convex inclusion morphologies.

For the mechanical error analysis, three different simple macroscopic virtual experiments are considered: horizontal tension, vertical tension, and simple shear, cf. Fig. 7. FE^2-simulations taking into account the target structure at the microscale are compared with FE^2-calculations focussing on the constructed SSRVEs. For this purpose, microscopic boundary value problems where a discretization by triangular finite elements with quadratic ansatz functions for the displacements are considered. Furthermore, plain stress conditions and periodic boundary conditions are applied. The individual constituents at the microscale are modeled by the simple J_2-plasticity model using a von Mises type hardening law, which is described above. The material parameters as given in Table 1 are used.

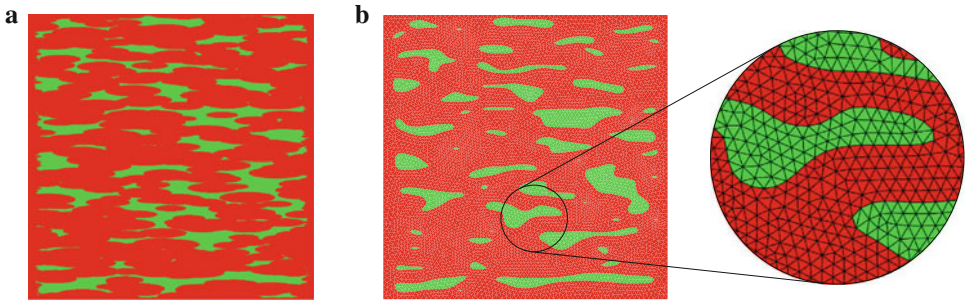

Fig. 5 Steps for the generation of the target structure: **a** result of the Boolean method and **b** smoothened inclusion phase boundaries with a section of the FE-discretization

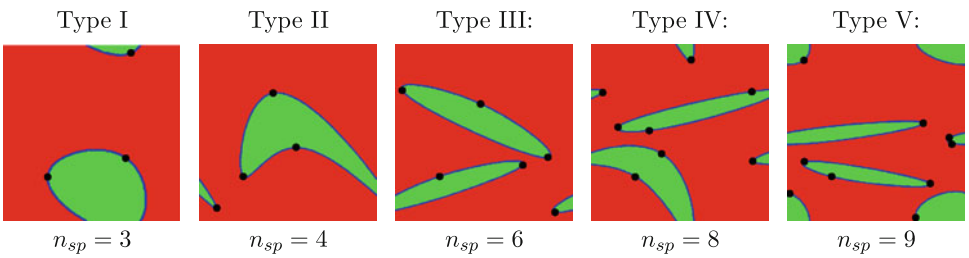

Fig. 6 Illustration of the five considered SSRVE types. The dots mark the sampling points of the splines

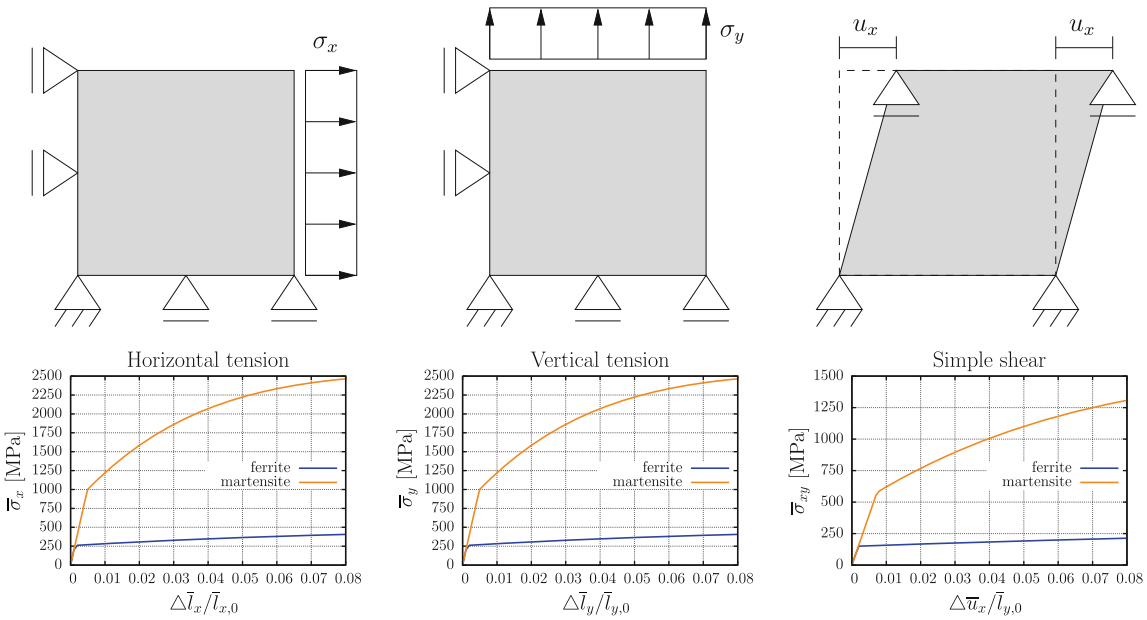

Fig. 7 Virtual macroscopic experiments of the pure matrix (ferrite) and inclusion material (martensite); at the microscale periodic boundary conditions are used

Table 1 Material parameters of the single phases

Phase	λ [MPa]	μ [MPa]	y_0 [MPa]	y_∞ [MPa]	η [–]	h [–]
Matrix	118, 846.2	79, 230.77	260.0	580.0	9.0	70.0
Inclusion	118, 846.2	79, 230.77	1000.0	2750.0	35.0	10.0

This leads to a much higher initial yield stress in the inclusions compared with the matrix, see Fig. 7 for the response of both constituents for the three virtual experiments. A similar behavior is usually observed for e.g. advanced high-strength steels.

As comparative mechanical measures, we consider the relative errors r_x, r_y and r_{xy} defined as the deviation of the resulting macroscopic SSRVE stress response from the target structure response at each evaluation point i for the three virtual experiments:

$$r_x^{(i)} = \frac{\overline{\sigma}_{x,i}^{\text{real}} - \overline{\sigma}_{x,i}^{\text{SSRVE}}}{\overline{\sigma}_{x,i}^{\text{real}}}, \qquad r_y^{(i)} = \frac{\overline{\sigma}_{y,i}^{\text{real}} - \overline{\sigma}_{y,i}^{\text{SSRVE}}}{\overline{\sigma}_{y,i}^{\text{real}}}, \qquad r_{xy}^{(i)} = \frac{\overline{\sigma}_{xy,i}^{\text{real}} - \overline{\sigma}_{xy,i}^{\text{SSRVE}}}{\overline{\sigma}_{xy,i}^{\text{real}}}, \tag{51}$$

where only values with non-vanishing denominator are taken into account. In addition to that, the average errors for each experiment

$$\widetilde{r}_{x,y,xy} = \sqrt{\frac{1}{n_{\text{ep}}} \sum_{i=1}^{n_{\text{ep}}} [r_{x,y,xy}^{(i)}]^2} \quad \text{with} \quad r_{x,y,xy}^{(i)} := r\left(\frac{i}{n} \triangle l_{\max}/l_0\right) \tag{52}$$

and the overall comparative measure

$$\widetilde{r}_{\varnothing} = \frac{1}{3}\left(\widetilde{r}_x + \widetilde{r}_y + \widetilde{r}_{xy}\right) \tag{53}$$

are taken into account for quantitative statements with respect to the performance of the individual SSRVEs. The total number of evaluation points i is denoted by n_{ep}.

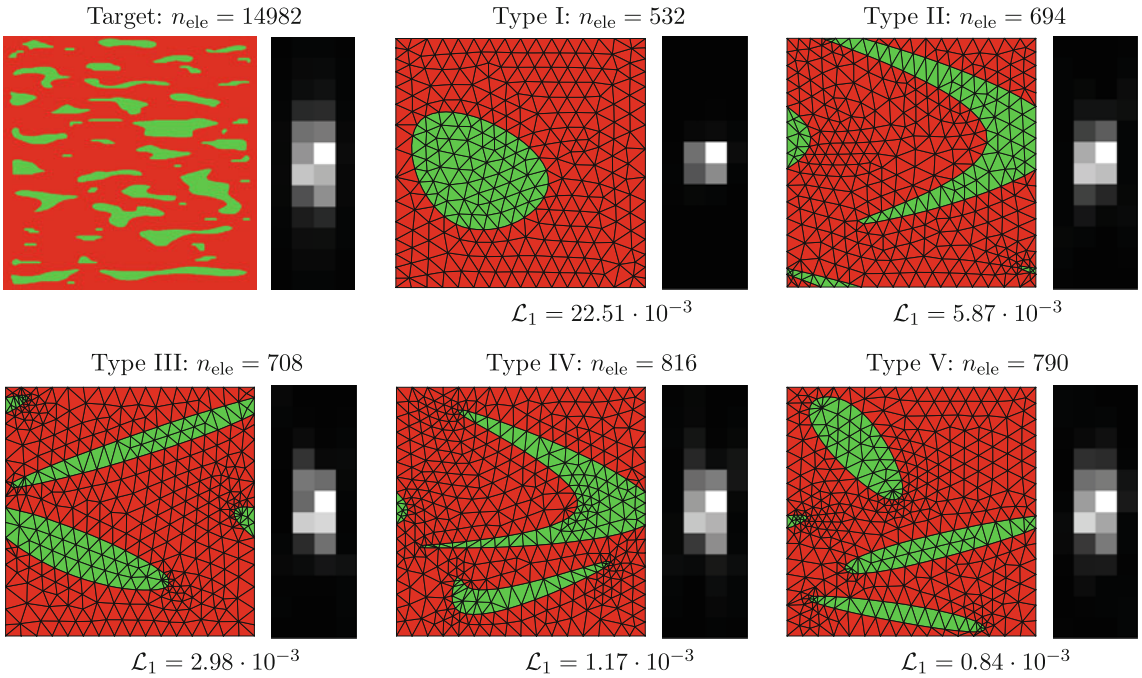

Fig. 8 Target structure and discretization of the SSRVEs with corresponding relevant area of the spectral density (right hand side) resulting from the minimization of $\mathcal{L}_1$

5.2 SSRVEs based on the volume fraction and the spectral density

As a first analysis, the spectral density is considered as the statistical measure describing the inclusion morphology, because it provides information regarding periodicity and the relative distances between the individual inclusions. Since also the phase fraction of the inclusions should reflect the one of the target structure, the associated least-square functional is additionally taken into account. This leads to the overall objective function

$$\mathcal{L}_1(\boldsymbol{\gamma}) = \omega_V \, \mathcal{L}_V(\boldsymbol{\gamma}) + \omega_{\text{SD}} \, \mathcal{L}_{\text{SD}}(\boldsymbol{\gamma}) \quad \text{with} \quad \omega_V = \omega_{\text{SD}} = 1, \tag{54}$$

wherein the individual least-square functionals are given by Eq. $(50)_{1,2}$. The weighting factors ω_V and ω_{SD} are set to one. In order to end up in a more efficient optimization procedure, a relevant area of the spectral density is defined. For this purpose, the complete spectral density of the target structure is computed and normalized before optimization. Since the target structure consists of 200×200 pixels, the number of entries in the complete spectral density is 200×200. Then, the spectral density is rebinned to the size 20×20, which seems to be reasonable because the important characteristics of the spectral density are maintained by rebinning. For a further enhancement of the numerical procedure, the minimal rectangular sub-area of the rebinned spectral density is identified, where no entry higher than a predefined threshold value of 0.02 is placed outside of the relevant area. Then only this rebinned relevant area of the spectral density with the size 4×12 enters the least-square functional. Finally, the objective function (54) is minimized with respect to the sampling point coordinates of the splines, which are assembled in $\boldsymbol{\gamma}$, by using the moving-frame algorithm proposed in Balzani et al. [1]. The resulting SSRVEs are automatically discretized in terms of the finite-element method and the realizations shown in Fig. 8 are obtained.

It can be observed that the number of finite elements n_{ele}, that is required for a suitable discretization, increases with increasing complexity of the SSRVE. Therefore, it seems that the number of required finite elements serves as some kind of estimation for the complexity of the inclusion morphology. In addition to that, the value of the computed minimum of the objective function is decreasing from $\mathcal{L}_1 = 22.51 \cdot 10^{-3}$ for Type I to $\mathcal{L}_1 = 0.84 \cdot 10^{-3}$ for Type V. This is kind of obvious since an increasing complexity of the inclusion morphology coincides more or less with an increase of the number of sampling points, which liberates the optimization problem given in Eq. (47). For the visual comparison, the rebinned relevant areas of the spectral density are provided on the right-hand side of the microstructure images. The spectral density of Type V obviously matches the spectral density of the target structure more accurately than Type I. For the mechanical

comparison of the SSRVEs with the target structure, the three virtual homogeneous experiments are calculated using the FE^2-scheme, and the stress–strain response shown in Fig. 8 is obtained. There, also the distribution of the relative mechanical error versus the strain is given.

For a better quantitative comparative analysis, the average errors, together with their standard deviation, and the overall mechanical comparative measures are computed and given in Table 2.

Table 2 Values of the objective function $\mathcal{L}_1$ and the errors $\widetilde{r}$ using the SSRVEs shown in Fig. 8, n_{dof} denotes the number of global degrees of freedom of the finite-element discretization

SSRVE	$\mathcal{L}_1[10^{-3}]$	$\mathcal{L}_V[10^{-6}]$	$\mathcal{L}_{\text{SD}}[10^{-3}]$	n_{dof}	$\widetilde{r}_x$ [%]	$\widetilde{r}_y$ [%]	$\widetilde{r}_{xy}$ [%]	$\widetilde{r}_{\varnothing}$ [%]
I	22.51	0.80	22.50	2,254	8.44 ± 1.96	0.66 ± 0.22	0.95 ± 0.22	3.35
II	5.87	27.16	5.84	2,914	2.56 ± 1.29	0.54 ± 0.26	9.12 ± 3.40	4.07
III	2.98	0.30	2.98	2,962	2.43 ± 0.86	1.72 ± 0.40	5.06 ± 2.07	3.07
IV	1.17	0.80	1.17	3,402	1.14 ± 0.39	0.97 ± 0.44	4.38 ± 1.85	2.17
V	0.84	39.76	0.80	3,290	0.14 ± 0.15	0.09 ± 0.06	3.08 ± 1.24	1.10

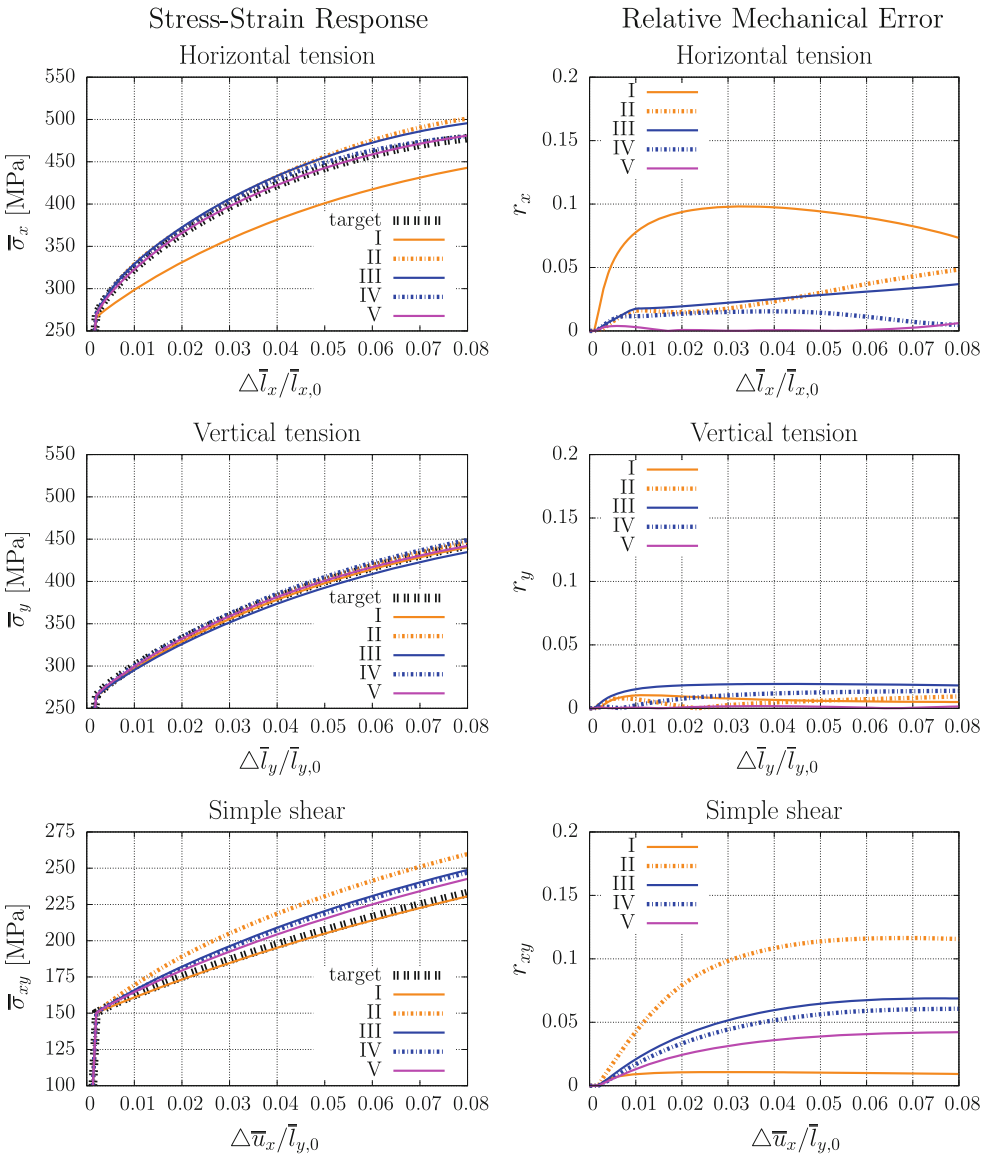

Fig. 9 Results of the virtual experiments using the discretizations of the SSRVEs (Fig. 8) based on $\mathcal{L}_1$. On the *left hand side* the Cauchy stresses are plotted versus strains, the *right hand side* shows the relative mechanical error

First, it is observed that the order of magnitude of the least-square function regarding the phase fraction $\mathcal{L}_V$ is twice to four times lower than the one regarding the spectral density $\mathcal{L}_{\mathrm{SD}}$. Since we are interested in SSRVEs where the phase fraction matches very well with the phase fraction of the target structure, the choice of $\omega_V = \omega_{\mathrm{SD}} = 1$ seems to be reasonable. Second, it can be observed that with increasing complexity (SSRVE Type I to Type V) the overall comparative error decreases in general, and Type V turns out to yield the best mechanical correspondence to the response of the target structure. However, when analyzing the individual average errors for the three virtual experiments a relatively high value of $\widetilde{r}_{xy} = 3.08$ is obtained for the simple shear test. Although the other two experiments of SSRVE Type V fit rather well the response of the target structure, the simple shear test is only partly represented accurately. This is also shown by the significantly deviating stress–strain curve shown in Fig. 9. In turn, the rather simple SSRVE Type I provides the best representation of the simple shear test, but the other experiments are reflected less accurately such that the overall comparative measure is $\widetilde{r}_{\varnothing} = 3.35$.

We conclude that possibly not enough statistical information is covered by the statistical measures considered in $\mathcal{L}_1$. Therefore, the subsequent section focusses on the additional incorporation of the lineal-path function.

5.3 Additional incorporation of the lineal-path function

Above, statistical measures have been taken into account that cover information regarding the phase fraction and the frequency of two points. The type of connectivity between two points is not captured yet. For this purpose, the lineal-path function is additionally considered in order to incorporate statistical measures of higher order. This leads to the objective function

$$\mathcal{L}_2(\boldsymbol{\gamma}) = \omega_V\,\mathcal{L}_V(\boldsymbol{\gamma}) + \omega_{\mathrm{SD}}\,\mathcal{L}_{\mathrm{SD}}(\boldsymbol{\gamma}) + \omega_{\mathrm{LP}}\,\mathcal{L}_{\mathrm{LP}}(\boldsymbol{\gamma}) \quad \text{with} \quad \omega_V = \omega_{\mathrm{SD}} = 1,\ \omega_{\mathrm{LP}} = 10, \tag{55}$$

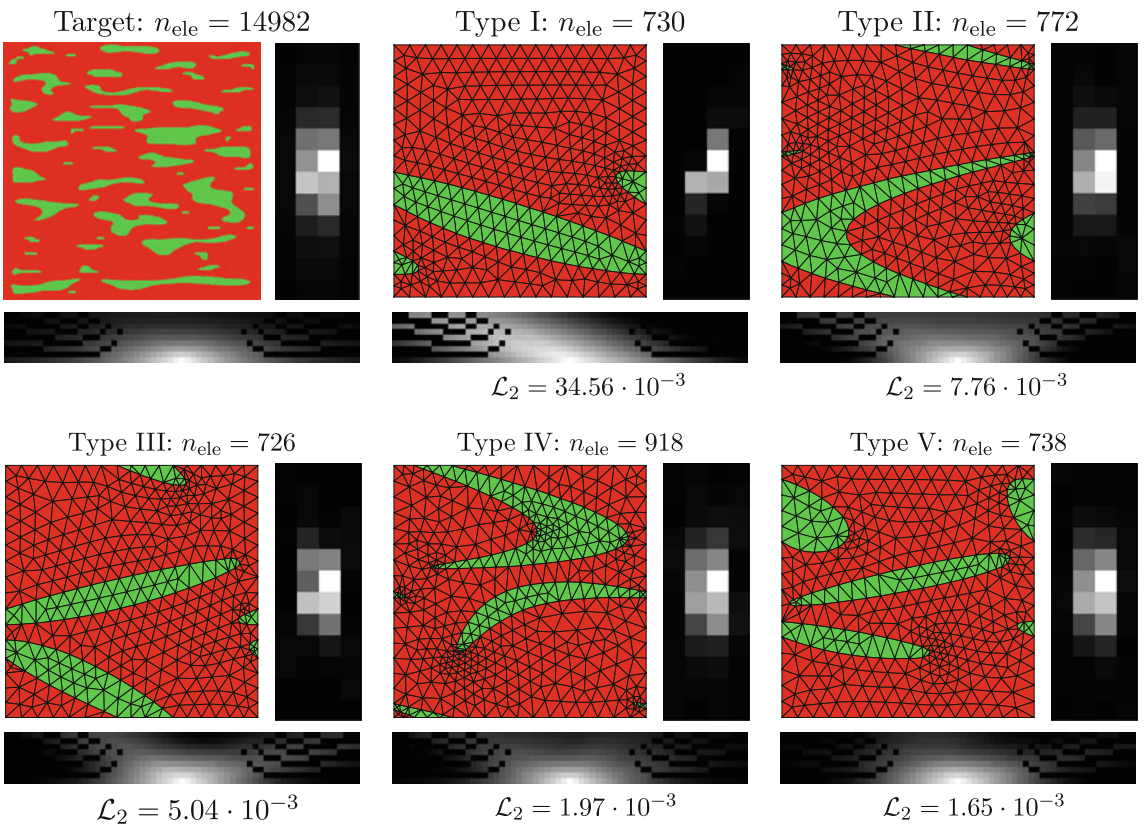

Fig. 10 Target structure and discretization of SSRVEs with corresponding relevant area of the spectral density (*right hand side*) and the lineal-path function (beneath the microstructure images) resulting from the minimization of $\mathcal{L}_2$; n_{ele} denotes the number of finite elements

wherein the weighting factors are set such that the order of magnitude of the individual least-square function values is in a reasonable range. The individual least-square functionals $\mathcal{L}_V$, $\mathcal{L}_{\mathrm{SD}}$ and $\mathcal{L}_{\mathrm{LP}}$ are given by in Eq. (50). To end up in a more efficient optimization procedure again the definition of a relevant area as described above is taken into account when comparing the spectral density in $\mathcal{L}_{\mathrm{SD}}$.

Due to the fact that computing the lineal-path function demands even more operations than computing the spectral density, an improved calculation method is required in this respect, too. Therefore, only a number of 40 line orientations distributed uniformly between the horizontal and the vertical direction are taken into account by an appropriate definition of the template. Furthermore, the size of the template which is considered for the computation of the lineal-path function of the SSRVEs can be significantly reduced by considering the typical length of inclusions in the target structure. For this purpose, the complete lineal-path function taking into account a template size $T_x \times T_y = 399 \times 200$ is computed for the target structure before optimization. Then, all values that are lower than a specified threshold value of 0.1 are set to zero. This defines the relevant template analogous to the way the relevant spectral density is identified. This leads to the fact that the size of the lineal-path function and the template size coincide, and the specific size $T_x \times T_y = 63 \times 9$ is considered.

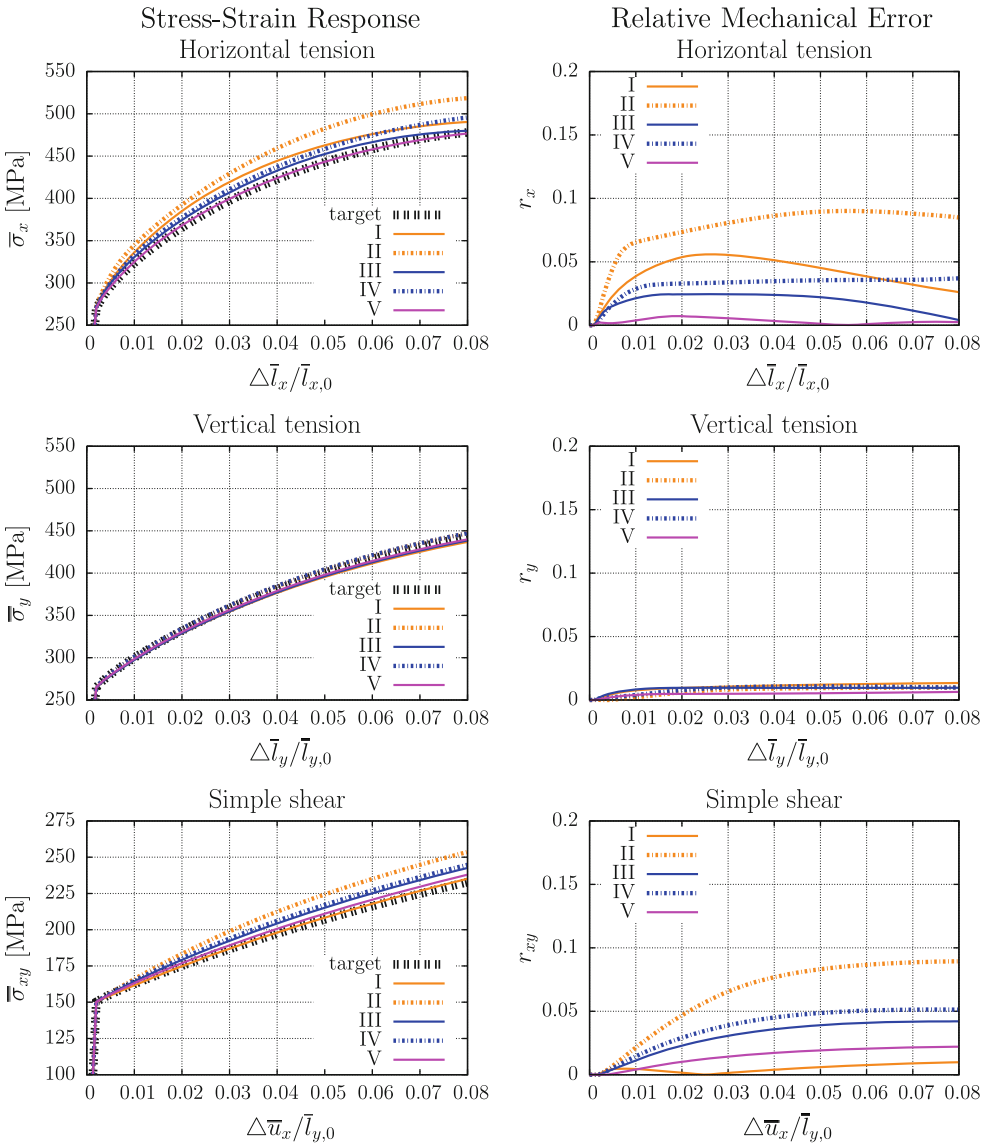

Fig. 11 Results of the virtual experiments using the discretizations of the SSRVEs (Fig. 10) based on $\mathcal{L}_2$. On the left hand side the Cauchy stresses are plotted versus strains, the right hand side shows the relative mechanical error

Table 3 Values of the objective function $\mathcal{L}_2$ and the errors $\widetilde{r}$ using the SSRVEs shown in Fig. 10, n_{dof} denotes the number of global degrees of freedom of the FE-discretization

SSRVE	$\mathcal{L}_2\,[10^{-3}]$	$\mathcal{L}_V\,[10^{-5}]$	$\mathcal{L}_{\text{SD}}\,[10^{-4}]$	$\mathcal{L}_{\text{LP}}\,[10^{-5}]$	n_{dof}	$\widetilde{r}_x$ [%]	$\widetilde{r}_y$ [%]	$\widetilde{r}_{xy}$[%]	$\widetilde{r}_{\varnothing}$ [%]
I	34.56	158.11	189.21	140.54	3,054	4.11 ± 1.28	1.05 ± 0.30	0.49 ± 0.30	1.88
II	7.76	9.08	44.70	31.98	3,238	7.74 ± 1.92	0.73 ± 0.32	6.39 ± 2.81	4.95
III	5.04	6.55	28.12	21.61	3,042	1.87 ± 0.67	0.89 ± 0.20	3.03 ± 1.29	1.93
IV	1.97	0.54	9.01	10.53	3,814	3.20 ± 0.78	0.86 ± 0.35	3.78 ± 1.58	2.61
V	1.65	6.55	7.04	8.85	3,082	0.32 ± 0.21	0.49 ± 0.13	1.47 ± 0.70	0.76

By using this improved procedure, the objective function (55) is minimized with respect to $\boldsymbol{\gamma}$, and the SSRVEs as illustrated in Fig. 10 are obtained. Again, a similar behavior of the objective function is observed. For increasing complexity of the SSRVE type, the value of the computed objective function minimum decreases from $\mathcal{L}_2 = 34.56 \cdot 10^{-3}$ for Type I to $\mathcal{L}_2 = 1.65 \cdot 10^{-3}$ for Type V. Obviously, the absolute values of the minimized objective functions for the individual SSRVE types are now slightly higher than for $\mathcal{L}_1$, because an additional least-square functional is taken into account. However, the comparison of the mechanical response remains to be analyzed. Let us first investigate the stress–strain response which is shown in Fig. 11.

There the distribution of the relative mechanical errors r_x, r_y and r_{xy} shows that SSRVE Type V seems to be the best SSRVE since the curve is below the curve of the other SSRVEs. In addition to that, the stresses obtained from SSRVE Type V are similar to the ones of the target structure for all three virtual experiments, also for the simple shear test, which is in contrast to the results obtained from minimizing $\mathcal{L}_2$. Hence, it seems that incorporating the lineal-path function additionally into the optimization problem leads to an improved overall mechanical representation of the target structure by the SSRVE. For a more detailed analysis, the average mechanical errors as well as the overall comparative measures are given in Table 3.
The most suitable SSRVE with the lowest overall comparative error is Type V. Although Type I leads also to a rather low value of $\widetilde{r}_{\varnothing}$, the average error for the horizontal tension test is rather high with $\widetilde{r}_x = 4.11$. In turn, SSRVE Type V yields low average errors for all three virtual experiments and yields the best approximation of the overall mechanical behavior of the target structure. Compared to the results obtained from minimizing $\mathcal{L}_1$, we can conclude that the incorporation of statistical measures of higher order seems to be promissing, since the additional incorporation of the lineal-path function yields significantly improved SSRVEs.

5.4 Inhomogeneous example

In this section, we compare the mechanical response of two macroscopically inhomogeneous FE^2-simulations, where the target structure and the most suitable SSRVE constructed in the previous section are considered at the microscale.

Figure 12 depicts the macroscopic boundary value problem of a radially expanded circular disk with a hole, the outer radius is $r_0 = 3.0$ cm, and the inner radius is $r_i = 0.5$ cm. We discretize the disk with

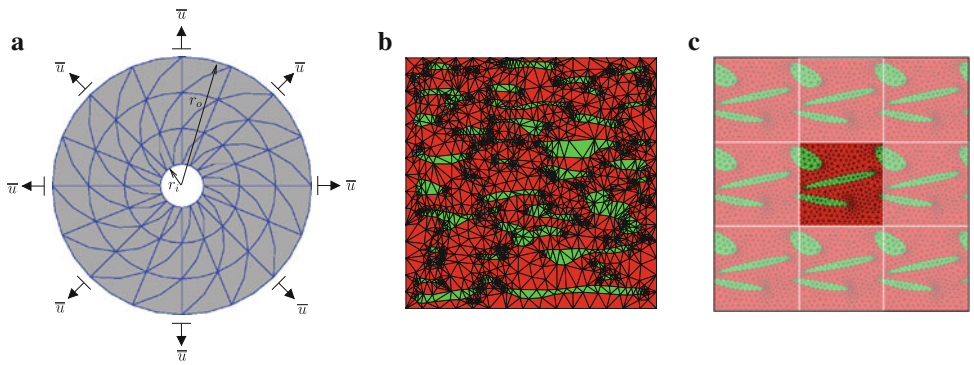

Fig. 12 **a** Macroscopic bvp: radially expanded circular disk with a hole ($r_i = 0.5$cm, $r_0 = 3.0$cm) discretized with 84 quadratic triangular elements under plain strain conditions; discretization of the **b** target structure with a reduced number of $n_{\text{ele}} = 5,452$ finite elements and **c** of the SSRVE Type V based on $\mathcal{L}_2$ (with its periodic expansion)

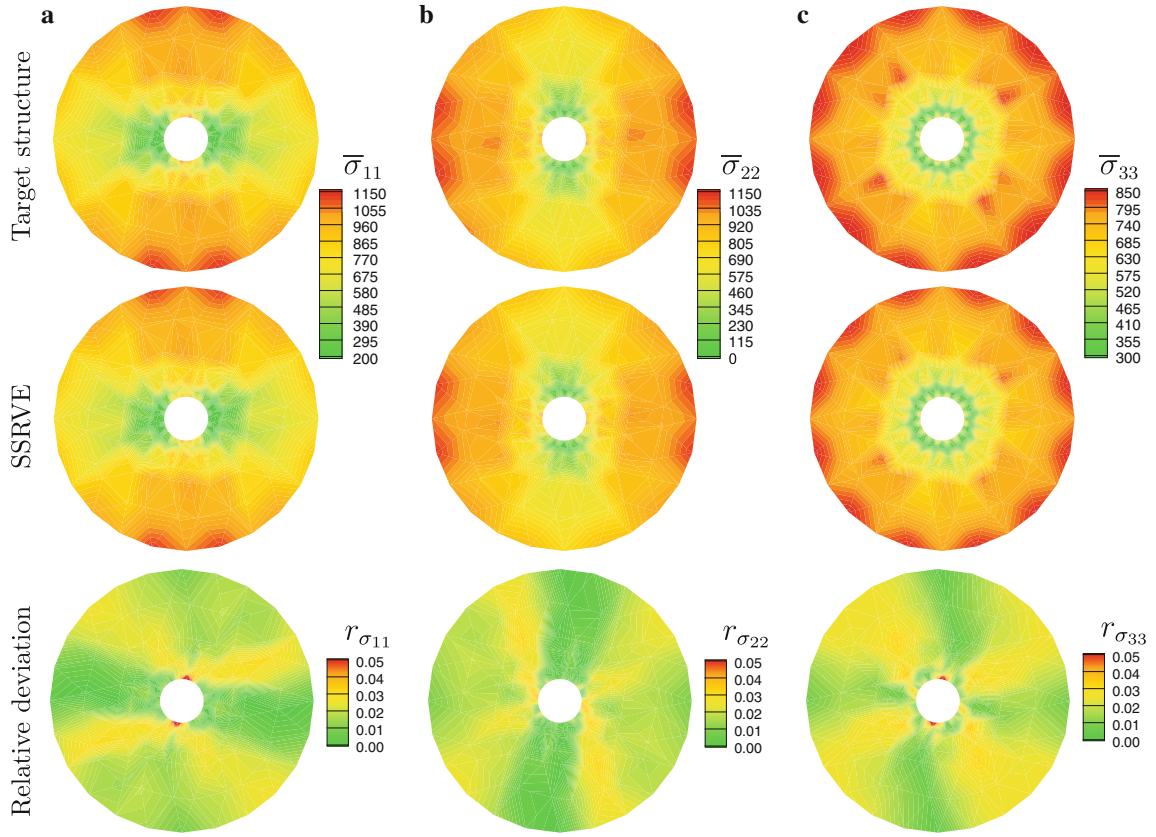

Fig. 13 Macroscopic stress distribution for **a** $\overline{\sigma}_{11}$, **b** $\overline{\sigma}_{22}$ and **c**) $\overline{\sigma}_{33}$ of the FE^2-simulations based on the target structure (*first row*) and the SSRVE (*second row*), and the relative deviations **a** $r_{\sigma_{11}}$, **b** $r_{\sigma_{22}}$ and **c** $r_{\sigma_{33}}$ comparing these two results (*third row*)

84 triangular elements with quadratic ansatz functions and consider plain strain conditions. During the simulation, the outer radius is driven by a radially orientated displacement condition from $\overline{u}(t = 0) = 0\,\text{mm}$ up to $\overline{u}(t = t_{\max}) = 1.6\text{mm}$. At the microscale, periodic boundary conditions are applied and at first the target structure is considered where a discretization with 5452 quadratic triangular elements (21930 degrees of freedom) is taken into account, see Fig. 12b. Second, the SSRVE Type V constructed by minimizing the objective function $\mathcal{L}_2$ is considered at the microscale, where a discretization with 738 quadratic triangular elements (3082 degrees of freedom) is addressed. In Fig. 12c, the finite element mesh of the considered SSRVE (regular colors) with its periodic expansion (brightened colors) of comparable size is shown. It is emphasized that for the FE^2-simulation only the SSRVE (regular colors) is taken into account since periodic boundary conditions are used.

Let us first investigate the macroscopic response of both simulations. Therefore, Fig. 13 shows the stress distributions $\overline{\sigma}_{11}$, $\overline{\sigma}_{22}$ and $\overline{\sigma}_{33}$ in the radially expanded disk at the final load step. When comparing the response of the second simulation, where the SSRVE is considered at the microscale (second row), with the first one based on the target structure (first row), a qualitatively and quantitatively similar stress response is observed at the macroscale. To get a quantitative estimation of the accordance, the relative deviation

$$r_{\sigma_{ii}}(\overline{\boldsymbol{x}}) = \left| \frac{\overline{\sigma}_{ii}^{\text{target}}(\overline{\boldsymbol{x}}) - \overline{\sigma}_{ii}^{\text{SSRVE}}(\overline{\boldsymbol{x}})}{\max\limits_{\overline{\boldsymbol{x}}} \left[\overline{\sigma}_{ii}^{\text{target}}(\overline{\boldsymbol{x}}) \right]} \right| \quad \text{with} \quad i = 1 \ldots 3 \tag{56}$$

is defined as a function of the position $\overline{\boldsymbol{x}}$ in the disk. This relative error describes the difference in the macroscopic stresses between both simulations relative to the maximal stress of the target structure at each macroscopic point. From the corresponding plots in the third row of Fig. 13, a relative deviation lower than 5% for all three stress components is observed. However, the maximum values of the relative deviation are rather localized; thus, a similar behavior of the macroscopic stress response can be concluded when comparing the

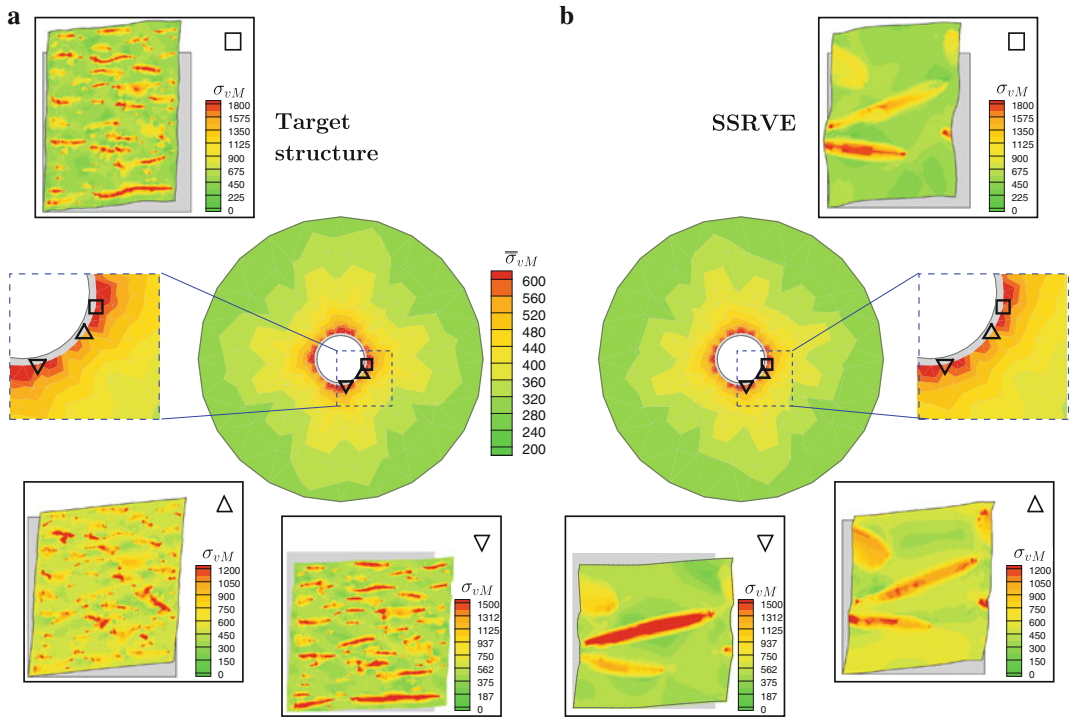

Fig. 14 Results of the FE^2-simulations based on the **a** the target structure and **b** the SSRVE with the von Mises stress distributions in the deformed microstructures for three selected positions. The *symbols in the upper right corner* of the images for the microscopic response represent the link to the macroscopic position; the *gray area* behind the microstructure indicates the undeformed configuration

response obtained for the SSRVE with the one based on the target structure. It is worthwhile mentioning that the macroscopic stress response shows a relatively low anisotropic character, although the virtual experiments in the last section show a significantly different behavior for the horizontal- and the vertical tension test. In Fig. 13c, the contour plot of $\overline{\sigma}_{33}$ is quite close to a rotational-symmetric distribution. A more pronounced anisotropic response can be expected for larger expansions.

Nevertheless, when comparing the microscopic stress distributions at different positions in the disk, a rather strong anisotropic character may be observed. To show this, Fig. 14 provides the von Mises stress distribution at the final load step in the disk ($\overline{\sigma}_{vM}$) as well as in the microstructures (σ_{vM}) at different macroscopic positions. For this multiscale comparison, three different macroscopic points are considered, which are located at the same distance from the inner boundary close to the inner radius of the disk. The maximum stress levels at the analyzed microstructures differ at the individual macroscopic points significantly from approximately 1,200 to 1,800 MPa due to the anisotropy of the RVEs. This represents a rather anisotropic character at the microscale although the macroscopic von Mises stress distribution is close to a rotational-symmetric one. In addition to that, the maximal stress levels at the microscales are significantly larger than at the macroscale. The latter two issues may play an important role with respect to failure initialization analysis, since the microscopically observable orders of magnitude and positions of maximum stress levels cannot be observed in purely macroscopic simulations.

If we compare the microscopic results related to the same macroscopic point of the simulation based on the SSRVE with the one based on the target structure, again similar stress levels are observed. Furthermore, the qualitative response at the microscale is similar, too. This accentuates the performance of the SSRVE and shows that it seems to be possible to approximate the response of random microstructures by much simpler SSRVEs. Finally, the profit with respect to the costs of data storage of the history variables is enormous when using SSRVEs compared with the chosen target structure. In the proposed approach, the needed data storage capacity is approximately reduced about 95 %, for the considered coupled micro-macro boundary value problem. Furthermore, the computation time is also significantly reduced. These are of course only rough estimates based on the considered discretizations.

6 Conclusion

In this contribution, a method is proposed for the construction of statistically similar RVEs (SSRVEs), which are characterized by a significantly less complexity than usual RVEs. These SSRVEs were based on the minimization of an objective function considering the difference of statistical measures computed for a random microstructure and for the SSRVE. The parameterization of the inclusion phase within the SSRVEs was performed by splines such that a periodification of the microstructure was realizable, and no intersections of the splines were allowed.

In a comparative analysis, different statistical measures, the volume fraction, the spectral density, and the lineal-path function, were investigated with respect to their applicability for the construction of SSRVEs. First, the resulting SSRVEs were tested in the virtual experiments, homogeneous tension in horizontal-/vertical direction and simple shear, and the mechanical response of the resulting SSRVEs were compared to the response of a target random microstructure. It turned out that by incorporating different statistical measures of higher order suitable SSRVEs can be constructed. This is reasonable since the spectral density covers periodic information, whereas the lineal-path function provides information regarding the type of connectivity of two points.

A further analysis was performed in order to study the applicability of the "best" SSRVE to represent the mechanical response of the target structure in a macroscopically inhomogeneous boundary value problem. The comparison of a FE^2-simulation, based on SSRVE and target structure simulations, showed that a similar macroscopic and microscopic response can be obtained. Hereby, it was shown that a SSRVE can be constructed based on the proposed method which captures the main attributes of a random microstructure. The fundamental advantage of the SSRVEs was that a much lower number of finite elements was required for the discretization at the microscale, which increases the computational efficiency enormously.

Acknowledgments The financial support of the "Deutsche Forschungsgemeinschaft" (DFG), research group MICROPLAST on "Analysis and Computation of Microstructures in Finite Plasticity", project No. SCHR 570/8-1, is gratefully acknowledged.

References

1. Balzani, D., Brands, D., Schröder, J., Carstensen, C.: Sensitivity analysis of statistical measures for the reconstruction of microstructures based on the minimization of generalized least-square functionals. In: Technische Mechanik (in press, 2010)
2. Balzani, D., Schröder, J., Brands, D.: FE^2-Simulation of microheterogeneous steels based on statistically similar RVE's. In: Proceedings of the IUTAM Symposium on Variational Concepts with Applications to the Mechanics of Materials, September 22–26, 2008, Bochum, Germany, (in press, 2009)
3. Beran, M.: Statistical continuum theories. Wiley, New York (1968)
4. Brekelmans, W.A.M., Smit, R.J.M., Meijer, H.E.H.: Prediction of the mechanical behaviour of nonlinear heterogeneous systems by multi-level finite element modelling. Comput. Methods Appl. Mech. Eng. **155**, S181–S192 (1998)
5. Bresenham, J.E.: Algorithm for computer control of a digital plotter. In: IBM Systems Journal 4 (1965), Nr. 1, S. 25–30. Reprinted in Interactive Computer Graphics, Herbert Freeman ed., 1980, and Seminal Graphics: Pioneering Efforts That Shaped The Field, Rosalee Wolfe ed., ACM SIGGRAPH, 1998
6. Brown, W.F.: Solid mixture permettivities. J. Chem. Phys. **23**, S1514–S1517 (1955)
7. Geers, M.G.D., Kouznetsova, V., Brekelmans, W.A.M.: Multi-scale first-order and second-order computational homogenization of microstructures towards continua. Int. J. Multiscale Comput. Eng. **1**, S371–S386 (2003)
8. Hill, R.: Elastic properties of reinforced solids: some theoretical principles. J. Mech. Phys. Solids **11**, S357–S372 (1963)
9. Klinkel, S.O.: Theorie und Numerik eines Volumen-Schalen-Elementes bei finiten elastischen und plastischen Verzerrungen, Universität Fridericiana zu Karlsruhe, Dissertation (2000)
10. Kröner, E.: Allgemeine Kontinuumstheorie der Versetzung und Eigenspannung. Arch. Rational Mech. Anal. **4**, S273–S334 (1960)
11. Kröner, E.: Statistical continuum mechanics. CISM Courses and Lectures Bd. 92. Springer, Wien (1971)
12. Lee, E.H.: Elasto-plastic deformation at finite strains. J. Appl. Mech. **36**, S1–S6 (1969)
13. Lu, B.L., Torquato, S.: Lineal-path function for random heterogeneous materials. Phys. Rev. A **45**, S922–S929 (1992)
14. Miehe, C.: Kanonische Modelle multiplikativer Elasto-Plastizität. Thermodynamische Formulierung und Numerische Implementation. Universität Hannover, Institut für Baumechanik und Numerische Mechanik, Bericht-Nr. F93/1, Habilitationsschrift (1993)
15. Miehe, C., Schotte, J., Schröder, J.: Computational micro-macro-transitions and overall moduli in the analysis of polycrystals at large strains. Comput. Mater. Sci. **16**, S372–S382 (1999)
16. Miehe, C., Schröder, J., Becker, M.: Computational homogenization analysis in finite elasticity: material and structural instabilities on the micro- and macro-scales of periodic composites and their interaction. Comput. Methods Appl. Mech. Eng. **191**, S4971–S5005 (2002)
17. Miehe, C., Schröder, J., Schotte, J.: Computational homogenization analysis in finite plasticity. Simulation of texture development in polycrystalline materials. Comput. Methods Appl. Mech. Eng. **171**, S387–S418 (1999)

18. Miehe, C., Stein, E.: A canonical model of multiplicative elasto-plasticity formulation and aspects of the numerical implementation. Eur. J. Mech. A/Solids **11**, S25–S43 (1992)
19. Ohser, J., Mücklich, F.: Statistical analysis of microstructures in materials science. Wiley, New York (2000)
20. Peric, D., Owen, D.R.J., Honnor, M.E.: A model for finite strain elasto-plasticity based on logarithmic strains: computational issues. Comput. Methods Appl. Mech. Eng. **94**, S35–S61 (1992)
21. Povirk, G.L.: Incorporation of microstructural information into models of two-phase materials. Acta Metallurgica **43**(8), S3199–S3206 (1995)
22. Schröder, J.: Homogenisierungsmethoden der nichtlinearen Kontinuumsmechanik unter Beachtung von Stabilitätsproblemen, Bericht aus der Forschungsreihe des Institut für Mechanik (Bauwesen), Lehrstuhl I, Habilitationsschrift (2000)
23. Schröder, J., Balzani, D., Richter, H., Schmitz, H.P., Kessler, L.: Simulation of microheterogeneous steels based on a discrete multiscale approach. In: Hora, P. (Hrsg.): Proceedings of the 7th International Conference and Workshop on Numerical Simulation of 3D Sheet Metal Forming Processes, pp. 379–383 (2008)
24. Simo, J.C.: A framework for finite strain elastoplasticity based on maximum plastic dissipation and the multiplicative decomposition: Part I. Continuum formulation. Comput. Methods Appl. Mech. Eng. **66**, S199–S219 (1988)
25. Simo, J.C.: Algorithms for static and dynamic multiplicative plasticity that preserve the classical return mapping schemes of the infinitesimal theory. Comput. Methods Appl. Mech. Eng. **99**, S61–S112 (1992)
26. Simo, J.C., Miehe, C.: Associative coupled thermoplasticity at finite strains: formulation, numerical analysis and implementation. Comput. Methods Appl. Mech. Eng. **96**, S133–S171 (1992)
27. Smit, R.J.M., Brekelmans, W.A.M., Meijer, H.E.H.: Prediction of the mechanical behavior of nonlinear heterogeneous systems by multi-level finite element modeling. Comput. Methods Appl. Mech. Eng. **155**, S181–S192 (1998)
28. Temizer, I., Wriggers, P.: On the computation of the macroscopic tangent for multiscale volumetric homogenization problems. Comput. Methods Appl. Mech. Eng. **198**, S495–S510 (2008)
29. Torquato, S.: Random heterogeneous materials. Microstructure and macroscopic properties. Springer, Berlin (2002)
30. Torquato, S., Stell, G.: Microstructures of two-phase random media I. The n-point probability functions. J. Chem. Phys. **77**, S2071–S2077 (1982)
31. Voce, E.: A practical strain hardening function. Metallurgica **51**, S219–S226 (1955)
32. Weber, G., Anand, L.: Finite deformation constitutive equations and a time integration procedure for isotropic, hyperelastic-viscoelastic solids. Comput. Methods Appl. Mech. Eng. **79**, S173–S202 (1990)
33. Zeman, J.: Analysis of Composite Materials with Random Microstructure, University of Prague, Dissertation (2003)